Quantitative Cryo-SEM and Fluorescence Microscopy Reveal Native Architecture and Matrix Complexity in *P. aeruginosa* Biofilms

Osondu-Chuka Goodness O.[1], Schandl Stephan[2], Guruprakash Subbiahdoss[1], Aleksandr Ovsianikov[2], Olivier Guillaume[2] and Reimhult Erik[1]

[1]Institute of Colloid and Biointerface Science, BOKU University, Muthgasse 11, Vienna 1190, Austria. [2] Institute of Materials Science and Technology, Technische Universität Wien, Vienna, Austria.

Abstract

Pseudomonas aeruginosa biofilms resist antibiotics and immune clearance through their biofilm organization, yet their native spatial organization and extracellular matrix (ECM) remain difficult to resolve. We compare air-drying, critical-point drying, and high-pressure cryogenic freezing for preparing *P. aeruginosa* biofilms for scanning electron microscopy (SEM) imaging. Only cryo-SEM preserved hydrated ECM ultrastructure, cellular morphology, and organization, whereas other methods caused severe distortions due to dehydration. Combining cryo-SEM with confocal laser scanning microscopy (CLSM) enabled quantitative spatial analyses with high resolution across large biofilm volumes. Nearest-neighbor distances, radial distribution functions, and Ripley's H-functions revealed broadly distributed cell spacings with a preferred distance of ~1 µm and only weak clustering in 4-day-old biofilms, challenging the view of biofilms as densely packed microcolonies. Mucoid and PAO1 strains exhibited distinct ECM ultrastructures and pronounced vertical stratification. This multiscale approach establishes cryo-SEM and CLSM as complementary tools for quantitative, high-fidelity biofilm analysis.

1 Introduction

Pseudomonas aeruginosa (PA) is a highly adaptable, opportunistic pathogen known for its ability to form robust biofilms, which contribute to persistent infections and antibiotic resistance.[1–3] Central to this resilience is the biofilm's extracellular matrix (ECM), a complex network of polysaccharides (alginate, Pel, and Psl), proteins, and extracellular DNA (eDNA) that acts as a robust protective barrier, enabling bacteria to withstand high antibiotic concentrations.[4,5] Alginate, in particular, is a hallmark of mucoid clinical isolates, often found in cystic fibrosis (CF) lungs, where it enhances biofilm resilience.[4,6–8] This resilience is primarily attributed to its ability to provide structural stability and act as a physical barrier against both antibiotics and host immune defenses.[4,6,8]

Overproduction of alginate leads to biofilms that are notably persistent and difficult to eradicate in clinical settings, making it a critical target for research.[6,7] Understanding the structural complexity of these biofilms is therefore essential for developing effective therapeutic strategies, as PA biofilm formation plays a central role in chronic infections, such as those associated with CF, burn wounds, and indwelling medical devices.[4,9]

Most of our understanding of biofilm formation and structure comes from detailed studies of a few species and strains, with *P. aeruginosa* PAO1 perhaps the best-studied.[3,10,11] It is important to note that even mucoid PA strains, despite belonging to the same species, form markedly different biofilms in terms of both biochemical composition and large-scale structure.[12,13] Still, a gap persists in our knowledge between molecular differences and global biofilm structure, including how cells and ultrastructure are organized; we must bridge these scales to understand the nano- to microscale functionality of biofilms.

This gap also hampers efforts to develop biofilm models for R&D.[14–16] In addition to studying clinical biofilms or biofilms grown *in vitro*, various *in vitro* models have been developed using alginate hydrogels to encapsulate bacteria.[17,18] These bacteria-loaded alginate hydrogel models mimic key features of the mucoid biofilm phenotype observed in clinical settings, particularly in CF lungs.[17,19] These models can elucidate the specific roles of molecular components, including alginate, in biofilm architecture and resilience, and provide standardized drug-screening platforms, but risk oversimplification if the structural organization is incorrectly reconstituted.

Electron microscopy has long been employed in biological research to visualize the ultrastructure of cells, bacteria, and tissues. Among its variants, scanning electron microscopy (SEM) has emerged as a valuable tool for visualizing PA biofilms, providing high-resolution images that reveal intricate surface morphology and spatial organization.[20–22] It has been particularly useful for examining biofilms formed on medical devices, where PA establishes resilient communities.[23,24] However, biofilm hydration and complex extracellular matrix composition, particularly with polysaccharide-rich regions,[25–27] pose a significant challenge in electron microscopy, where traditional methods require sample dehydration for imaging in vacuum, leading to structural collapse and loss of integrity.[28–30] This collapse results from the removal of water in the structure and from the changed energetics of structures favored by hydration and ionic interactions, which are no longer in equilibrium when the water is removed. Membranes and polysaccharides undergo significant reorganization, shrinkage, and collapse upon water removal, distorting their native architecture and functional properties.[26,31,32] Specialized sample preparation and imaging techniques are therefore

necessary to visualize the native architecture of biofilms without introducing structural artifacts.[21,26,33] Additionally, standard SEM techniques are limited to imaging the surface of biofilms, which restricts our ability to understand the organization within the biofilm, as it may differ significantly from the surface structure and cell distribution. A reasonable assumption is that biofilms change their composition as they grow, thereby altering their structure with increasing distance from the substrate.[34,35] Techniques that expose the organization within the biofilm to compare it to the structure in the presumably faster-growing top part are therefore essential for understanding biofilm architecture.

Several preparation techniques have been developed to address the challenge of imaging hydrated biological structures.[25,26,29] Controlled drying by the critical-point drying (CPD) method has been widely used to preserve cellular morphology; however, it introduces artifacts in highly hydrated structures, such as biofilms.[36,37] Fixation, commonly used to stabilize biological samples for electron microscopy, presents another limitation. While chemical fixatives such as aldehydes and osmium tetroxide cross-link cellular components, they do not preserve the organization of polysaccharides and other sugar-rich structures.[30,38] The dehydration steps required for fixation-based protocols further disrupt biofilm organization and shrink structures, making capturing the biofilm ultrastructure dubious. [30,36,37]

Cryo-scanning electron microscopy (cryo-SEM) offers a promising solution for preserving biofilm structures in their near-native state.[28,29] Rapid freezing of samples within milliseconds prevents ice crystal formation. Cryo-SEM preserves hydration by maintaining samples in a frozen, vitrified state, enabling high-resolution imaging of biofilms with minimal structural distortion.[26,39] This approach minimizes artifacts and provides a more accurate representation of biofilm morphology, capturing delicate extracellular polymeric substances (EPS) and cellular arrangements that are often lost with traditional preparation methods.[26,28,40] High-pressure freezing (HPF) applies mechanical pressure during freezing to reduce ice crystal growth, enabling deeper penetration of the freezing process in mm-thick biofilm samples.[41–43] After cryo-freezing, the sample can be split open by various methods to expose a surface on or within the biofilm. [29,44,45] Nevertheless, the resulting split surface lacks contrast for imaging the ultrastructure, although large structures such as membranes and fibers are exposed. Improved contrast is achieved by depositing a thin carbon-metal film, typically at an angle, which also stabilizes the interface for imaging. In an additional step before carbon-metal film deposition, freeze-etching, which involves the controlled sublimation of a small amount of surface ice before imaging, can further enhance contrast and reveal structural details that would otherwise

be obscured by frozen water layers.[29,46,47] These cryo-methods, when combined with SEM, enable researchers to explore biofilm architectures in their hydrated state at unequaled resolution, potentially offering novel and critical insights.

CLSM has long been an indispensable tool for investigating biofilm structure and organization in 3D,[48,49] and is an ideal complement to cryo-SEM. CLSM enables visualization of cellular distribution across the full biofilm thickness, making it particularly well-suited for quantitative structural analysis.[50–52] Unfortunately, its resolution is diffraction-limited, putting ultrastructure analysis beyond reach and making analysis of densely packed bacteria in biofilms challenging. However, by applying statistical image analysis tools, bacterial cell organization in biofilms can be quantified. By segmenting 3D CLSM image stacks into defined volumetric elements, it becomes possible to extract layer-resolved metrics describing how cells are distributed and organized along the biofilm thickness.[53,54] Such analyses provide insight into structural anisotropy and vertical heterogeneity, which are critical features of the biofilms but are not readily accessible through using only 2D imaging techniques.[53,54]

The aim of our work was to demonstrate the necessity of cryo-preparation methods to reveal true biofilm organization and ultrastructure, and to leverage the combination of cryo-SEM and CLSM for quantitative image analysis of PA biofilms in their native state. By minimizing preparation-induced artifacts and revealing the native structural organization of cells and ECM, we seek to provide missing structural information beyond genetic and biochemical data that could prove instrumental in elucidating how biofilms form and grow, establishing the causes of biofilm tolerance to antibiotics, and developing more effective anti-biofilm strategies.

2 Results and Discussion

2.1 Cryo-SEM Preserves Alginate Biofilm Model and Mucoid Biofilm Structures in Contrast to Dehydration Methods

SEM is a vacuum-based imaging technique, and structural observations of naturally hydrated systems can vary with sample preparation methods, which is highly relevant to SEM use in biofilm research.[26,39,55] However, because no standardized protocol exists for high-fidelity visualization of hydrated biofilms,[26,30,39] our initial objective was to establish a method capable of preserving native ultrastructure. We first focused on defining the baseline appearance of PA biofilm models (suitable for high-throughput screening of antibiotic activities) and native mucoid PA biofilms (bacterial cells

126 and the surrounding matrix) using cryo-SEM. Biofilm images obtained after cryo-preparation were
127 compared with those obtained after conventional preparation techniques, causing dehydration.

128 Alginate hydrogels proposed as models for antibiotic testing on mucoid PA biofilms [9,56,57] displayed
129 notable differences in structure depending on the sample preparation method: air-dried (AD),
130 critical-point-dried (CPD), or HPF-cryo-prepared. In the AD and CPD samples (**Figure 1a and b**),
131 the alginate hydrogels appeared spongy and compact, with wrinkled morphology. These features
132 are consistent with dehydration-induced artefacts rather than native structure. Pore sizes generally
133 ranged from ~0.1 – 0.35 µm (**Figure S1)**. Similar results have been reported in the literature where
134 CPD alginate gels exhibited irregular internal pore spaces that increased in size with decreasing
135 alginate concentration.[58] The observed pore diameters ranged from 0.2 to 3.0 µm within a 0.3%
136 (w/v) gel, and from 0.1 to 1.0 µm within a 0.6% (w/v) gel.[58] On the other hand, the cryo-prepared
137 sample (**Figure 1**c) retained a markedly more hydrated and native-like appearance, maintaining a
138 porous network (~0,3 µm – 0,55 µm) (**Figure S1**), which had significantly larger pores than both
139 the AD and CPD prepared samples ($p \leq 0.05$). However, we cannot rule out that the observed pore
140 size already partly reflects sublimation of water during the minimal etching used to provide imaging
141 contrast. This is likely, given the orders of magnitude smaller pore sizes obtained from rheological
142 testing and diffusion studies as reported in our previous publications.[9,59]

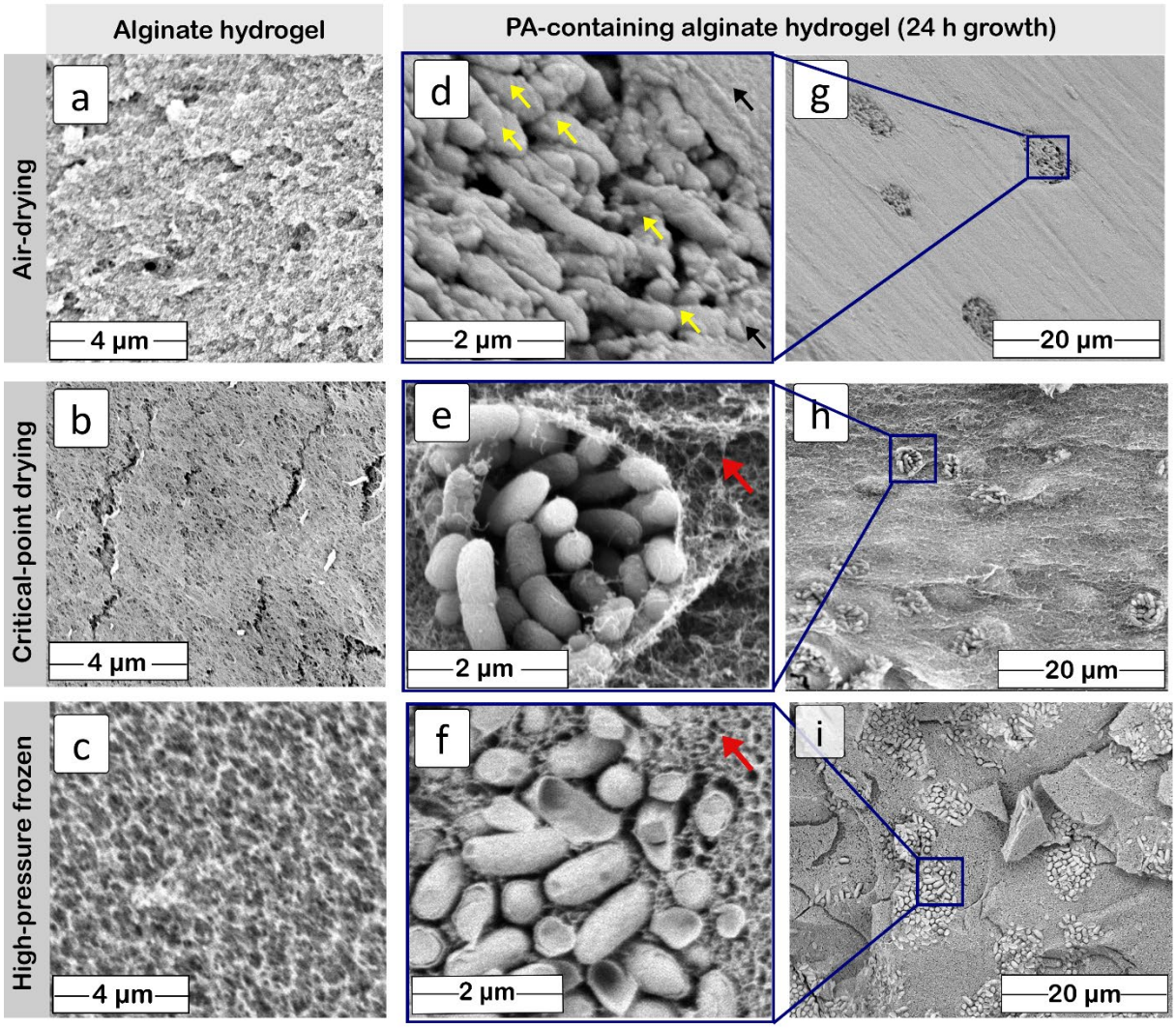

Figure 1: SEM micrographs depicting cross-sections of acetylated alginate hydrogels and biofilm models. Samples were prepared for imaging using air-drying (a, d, and g), critical-point drying (b, e, and h), and high-pressure freezing (etching time: 20 s – control alginate hydrogel, 40 s – PA-containing alginate hydrogel) (c, f, and i). a – c) acetylated alginate hydrogels, d – i) PAO1 encapsulated in acetylated alginate and grown overnight at 37 °C (biofilm models). The bacterial cells have been false-colored green for visibility.

In the next step, PA-containing alginate hydrogels (3D biofilm models) that closely mimic PA mucoid biofilms were studied after 24 h incubation at 37 °C.[56] These models are important for high-throughput testing and mechanistic testing of antibiotics, by replicating key features of biofilms reproducibly *in vitro*,[19,57,60] avoiding the inherent variability in native biofilms that hamper statistical testing. In AD and CPD-prepared samples (**Figure 1** d, e, g, and h), the surrounding alginate matrix was observed to be compact (black arrow) and spongy (red arrow), respectively.

156 Bacterial cells also exhibited distorted morphologies (yellow arrows) in AD-prepared samples,
157 which we attribute to the harsh dehydration process. In contrast, the cryo-prepared sample (**Figure**
158 **1f and i**) revealed the high-resolution morphology of the alginate matrix and PA microcolonies,
159 with cells embedded in a hydrated, mesh-like alginate gel (red arrow). There was no obvious
160 remodeling of the alginate matrix visible outside the microcolony.

161 Comparable insights into the growth and distribution of PA microcolonies in alginate hydrogel were
162 obtained by Sønderholm *et al*., who studied PA aggregate formation within alginate bead models
163 using confocal laser-scanning microscopy (CLSM).[57] However, the CLSM-based approach **(Figure**
164 **S2)**, while powerful for studying large-scale spatial organization and metabolic gradients in
165 hydrated systems, lacks the ultrastructural resolution provided by cryo-SEM. Our imaging results
166 reveal the fine details of bacterial morphology and the alginate matrix surrounding the bacteria. By
167 resolving these structural features in their hydrated, near-native state, cryo-SEM enables a more
168 accurate and reliable assessment of how these model biofilms respond to antimicrobial therapy, and
169 how therapeutics may remodel or disrupt individual matrix components. Hence, we can address a
170 key question in the study of antibiotic interactions with biofilm ECM models: do such printed
171 biofilms capture the ultrastructural organization of the ECM in native biofilms? Complex structural
172 matrix properties in native biofilms could influence antibiotic penetration and treatment
173 outcomes,[15,61,62] making an accurate visualization of true biofilm architecture biologically and
174 clinically relevant.

175 **Figure 2** shows representative SEM and CLSM images of 4-day-old mucoid PA biofilms grown on
176 type A gold carriers and glass, respectively. Biofilms on sample carriers were prepared for imaging
177 using different methods: air-drying (AD), critical-point drying (CPD), and HPF-cryo-prepared.
178 Rod-shaped PA cells were apparent in the dehydrated samples; however, the cells from the AD
179 samples (**Figure 2a**) appeared tightly packed in the imaged region, while cells from CPD-prepared
180 samples (**Figure 2b**) had an uneven spatial organization in the biofilm.
181 In contrast, in cryo-prepared and cryo-SEM imaged samples (**Figure 2c**), PA appear spatially
182 organized as individual cells, embedded in a voluminous ECM. The cryo-prepared biofilms retain
183 a highly hydrated ECM structure that closely reflects their native state and exhibits a distinctly
184 different morphology from that observed in samples prepared by other techniques or in the cryo-
185 prepared alginate model. A similar spatial distribution of cells was observed by CLSM imaging
186 (**Figure 2d**).

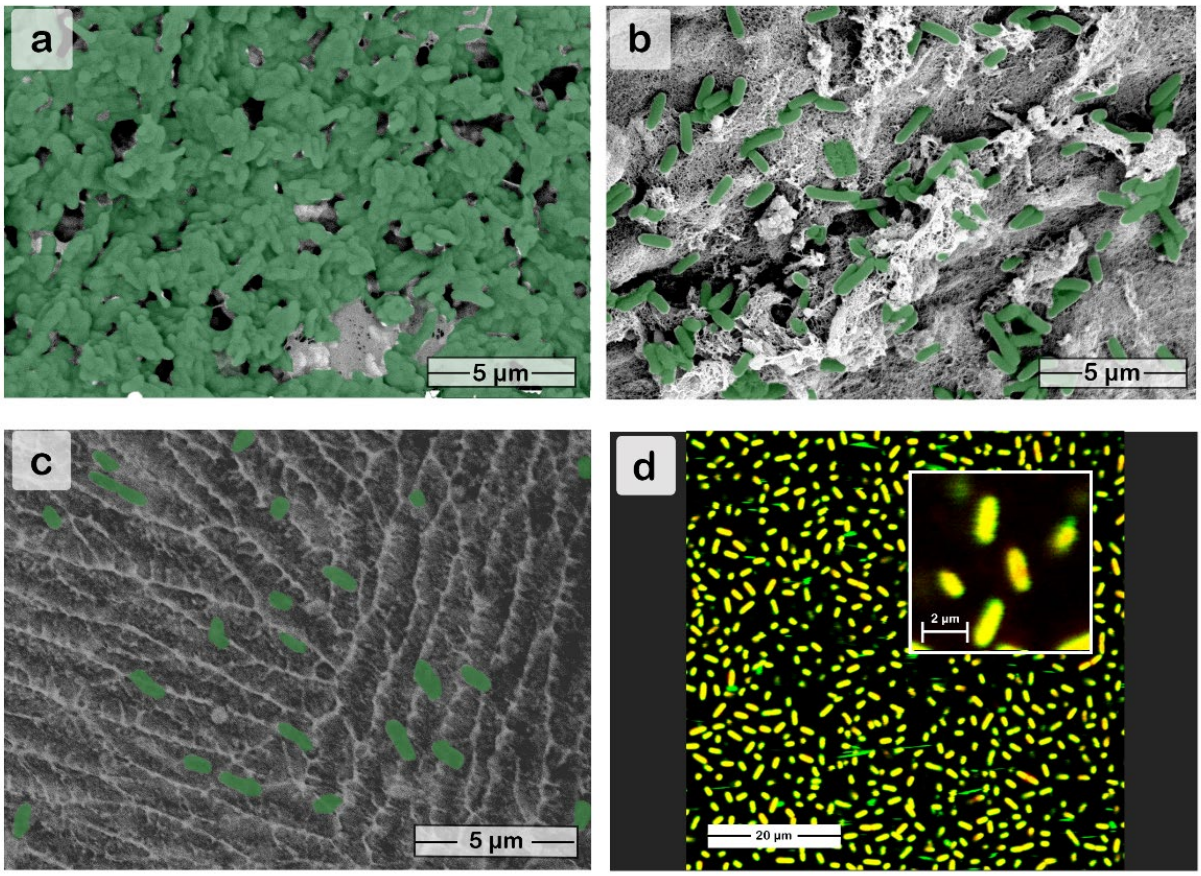

Figure 2: Effect of sample preparation on the spatial distribution of cells in 4-day-old mucoid PA biofilms. a) air-dried biofilm, b) critical-point dried biofilm, c) high-pressure frozen biofilm, and d) Syto9/PI-stained biofilm imaged by CLSM. The bacterial cells in a – c have been false-colored green for visibility (**Figure S16**).

The spatial organization differences observed across sample-preparation methods applied to mucoid PA biofilms highlight important implications for interpreting biofilm organization and structure. As described in other studies,[55,63] AD and CPD methods can provide a clear visualization of bacterial cells, but these preparation methods misrepresent the native biofilm structure. The collapse and shrinkage observed in mucoid PA samples upon dehydration result in structural artifacts, including cell clustering and loss of ECM ultrastructure. In contrast, HPF-prepared samples imaged by cryo-SEM conserve the organization (**Figure 2** and **S3)**. This finding is consistent with the work of Alhede *et al*., who compared cryo-preparation methods with CPD and concluded that cryo-preparation of PAO1 biofilms preserves the matrix structure.[64] One striking novel observation from our study is the spatial organization and distribution of PA cells. As exemplified in **Figure 2**c, we find that 4-day-old mucoid PA biofilms consist of individual bacterial cells that are spatially separated and embedded within a continuous and protective ECM.

2.2 Cryo-SEM Enables Quantitative Determination of the Spatial Distribution and Organization of Cells in *P. aeruginosa* Biofilms

To quantify the distinct spatial organization observed in the cryo-prepared mucoid PA biofilms, we calculated the centroid nearest-neighbor distances (NND) and the radial distribution function (RDF; $g(r)$) for the distribution of cells obtained from multiple cryo-SEM samples (**Figure 3 and Figure 4**, respectively) for different strata within the biofilm: bottom (~1 – 5 µm closest to the substrate), bulk (~5 – 45 µm from the substrate), and top (~1 – 5 µm closest to the bulk fluid).

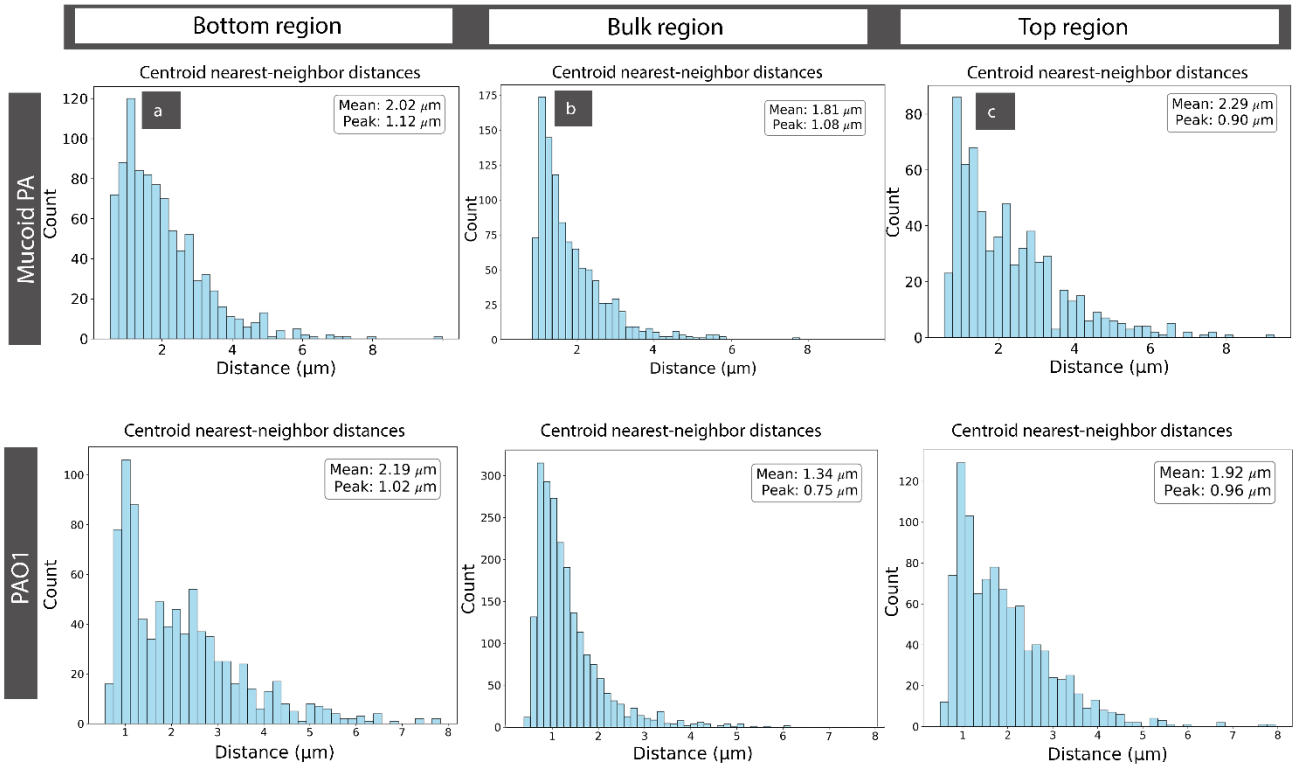

Figure 3: Region-specific distributions of centroid nearest-neighbor distances within PA biofilm. Histograms show nearest-neighbor distances for bacterial cell centroids in (a) bottom, (b) bulk, and (c) top mucoid PA biofilm regions, and (d) bottom, (e) bulk, and (f) top PAO1 biofilm regions.

The NND histograms for mucoid PA biofilms (**Figure 3a – c)** show that, although the peak distance is ~1 µm for every stratum, the mean distance between neighboring bacteria is ~2 µm, with a significant tail at distances over 4 µm and a broader distribution for bacteria in the top and bottom sections of the biofilms. This is also reflected in larger mean NNDs for the top and bottom.

The RDF (**Figure 4a – c**), on the other hand, provides a statistical description of how cell density varies with distance from each cell. In contrast to simple density measurements or the NND, the RDF captures whether cells are randomly distributed or arranged with characteristic spacings. A

222 value of $g(r) = 1$ corresponds to a random (Poisson) distribution of bacteria with the same overall
223 density as observed in the sample, whereas pronounced peaks indicate preferred intercellular
224 spacings. RDF analysis is widely applied in soft-matter physics to analyze colloidal systems.[65,66]

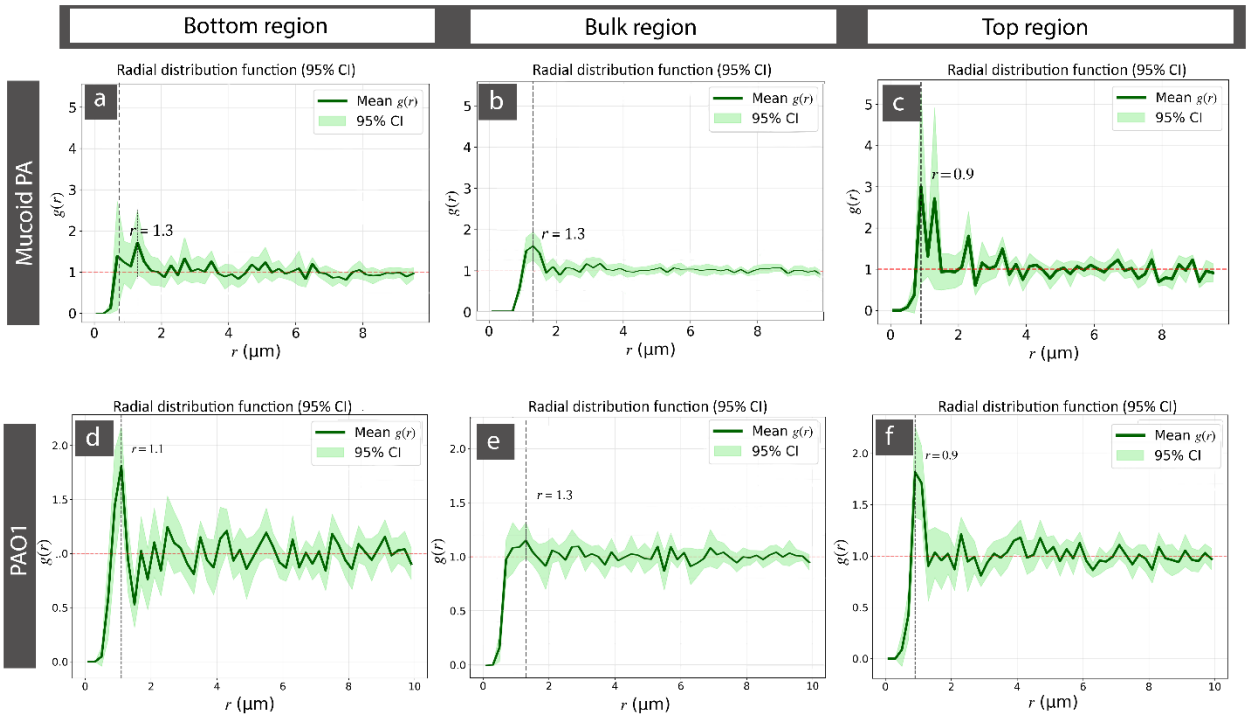

225

226 **Figure 4:** Averaged radial distribution function (RDF) analysis of PA biofilm spatial organization
227 in cryo-SEM biofilm images, illustrating bacterial density as a function of radial distance from each
228 cell center. a – c) RDF from the bottom, bulk, and top regions of mucoid PA biofilms, respectively.
229 d – f) RDF from the bottom, bulk, and top regions of PAO1 biofilms, respectively. A total of ≥10
230 images per region were selected for calculating the average RDF. The green line represents the
231 mean RDF, while the shaded area indicates the 95% confidence interval (CI). The black dotted line
232 represents the most probable distance at which a cell finds a neighbor.

233 In the mucoid PA biofilms analyzed, RDF profiles from the bottom and bulk regions (**Figure 4**a
234 and b) exhibited a strong first peak at ~1.3 μm, indicating a well-defined preferred spacing between
235 neighboring cells. This distance suggests that direct cell–cell contact is largely avoided, with cells
236 separated by extracellular material. The fluctuations around $g(r) = 1$ for $r > 2$ μm indicate that
237 bacteria only order or cluster at short ranges. The observations regarding the top-layer NND data
238 are given a statistical basis from the RDF (**Figure 4**c), showing a much higher likelihood of finding
239 another bacterium at a distance between 0.9-1.5 μm, as well as with lower likelihood at multiples

of these distances up to 4 µm, but farther away, a near random likelihood with low fluctuations. The order in the bottom and the bulk layers is significantly lower.

Having observed distinct cell–cell spacing in mucoid PA biofilms, we also examined PAO1 biofilms prepared under the same cryo-SEM conditions as the mucoid PA biofilms. Similar NNDs and RDFs were observed for PAO1 biofilms (**Figures 3d – f and 4d – f respectively**). While the peak and mean distances between cells were ~1 µm and ~2 for every stratum, the RDFs of the bottom, bulk, and top regions exhibited first strong peaks at 1.1 µm, 1.3 µm, and 0.9 µm, respectively.

The spatial organization of cells in biofilms can be analyzed at lower resolution, but for larger volumes and higher numbers of bacteria, using CLSM. CLSM-derived RDF measurements were generated from three-dimensional image stacks acquired under consistent imaging conditions across >6 biological replicates. Live-dead staining of the bacteria and constraints in terms of cell shape from the cryo-SEM analysis were used to segment the fluorescence and fit bacterial cells as cylinders, variable in size and orientation (**Figure** 5).

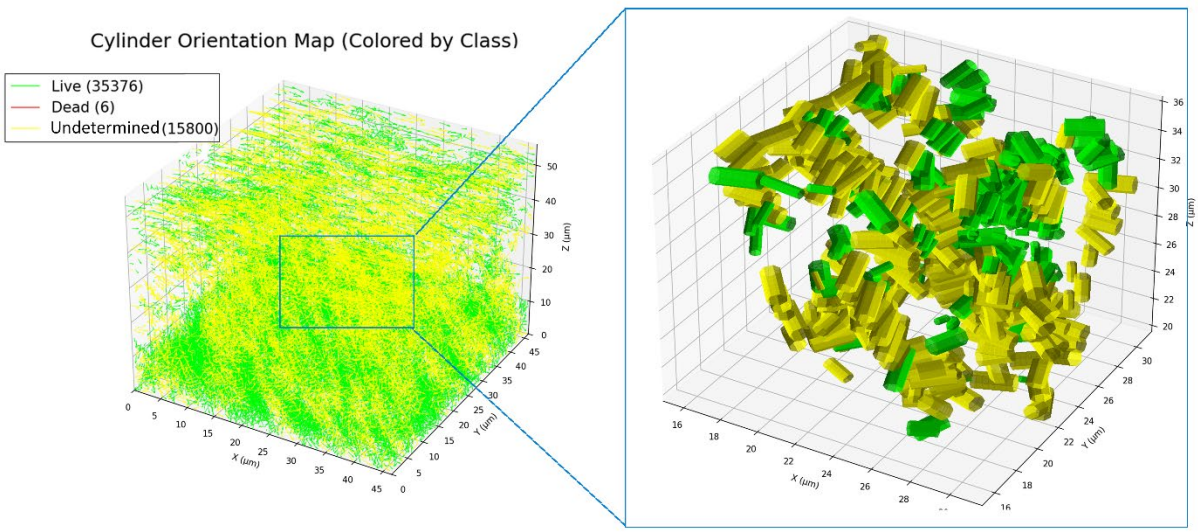

Figure 5: Three-dimensional orientation map of bacterial cells within the PA biofilm. Individual bacteria are represented as cylinders positioned and colored according to viability class (live (predominantly green), dead (predominantly red), and undetermined (strongly green and red)). The visualization highlights the spatial organization and orientation of cells across the biofilm volume.

260 The centroid coordinates of the cylinder-fitted bacteria were extracted and used to calculate the
261 RDF in cylindrical coordinates, separating the radial (x-y) plane comparable to the cryo-SEM cross-
262 section images, and the perpendicular z-axis. These analyses were represented as heatmaps (**Figure**
263 **S4)**. To match the RDF of the SEM images, only the g(r,z=0) was compared.

264 In the mucoid PA strains, the average first-peak values for $g(r,z=0)$ were approximately 0.85 ± 0.13
265 µm (bottom region), 0.742 ± 0.07 µm (bulk region), and 0.746 ± 0.09 µm (top region), respectively,
266 indicating a relatively consistent preferred spacing across the biofilm depth. In PAO1 biofilms, the
267 corresponding average peak positions were approximately 1.11 ± 0.2 µm (bottom), 0.86 ± 0.09 µm
268 (bulk), and 0.89 ± 0.14 µm (top), respectively. Only for PAO1 was a significant ($p \leq 0.05$) difference
269 in peak position between the bottom and the bulk found. The larger confidence intervals in the
270 bottom and top regions of the biofilms for both strains indicate greater heterogeneity in preferred
271 spacing for these regions across the imaged samples. The systematically shorter preferred distances
272 obtained from CLSM than cryo-SEM suggest slightly closer cell packing in the fluorescence-based
273 measurements. This is likely attributable to methodological differences between the two imaging
274 approaches. CLSM data are limited by diffraction-limited resolution, necessitating algorithmic
275 distinction between closely spaced bacteria. This can misidentify a single large, diffuse bacterium
276 as two, or position two closely spaced bacteria closer together than their actual distance because of
277 their overlapping point-spread functions. Such errors will underestimate true average intercellular
278 distances. In contrast, cryo-SEM provides superior resolution, easily enabling us to distinguish
279 individual bacteria.

280 The near equidistance of *P. aeruginosa* cells across all strata of the biofilms implies that the
281 mechanism that separates cells after division is either confined to the top layer of a growing biofilm
282 and conserved as the biofilm expands or operates similarly throughout. However, the latter
283 alternative would require active migration toward the biofilm surface if the cell density is similar
284 throughout the biofilm.

285 2.6 Ripley's $H(r)$ reveals strain-specific spatial clustering and organization in PA biofilms

286 Ripley's H-function provides a statistical measure of whether clustering is observed and, if so, how
287 large such clusters are, by integrating the RDF and normalizing it by the distance from each
288 bacterium. Hence, positive values of $H(r)$ indicate clustering relative to a random distribution of
289 bacteria, whereas negative values indicate fewer bacteria found at this distance than expected.
290 Calculating $H(r)$ from the CLSM data, mucoid and PAO1 biofilms exhibited weakly positive $H(r)$
291 values at distances up to 10 µm across all samples and layers (**Figure 6**), demonstrating that cell

distributions in both strains were intrinsically non-random and dominated by local correlations. In both biofilm types, pronounced $H(r)$ maxima occurred at length scales of approximately 1–2 µm, with the highest peaks in the top region. However, differences emerge when clustering behavior is examined across larger spatial scales and along the biofilm depth.

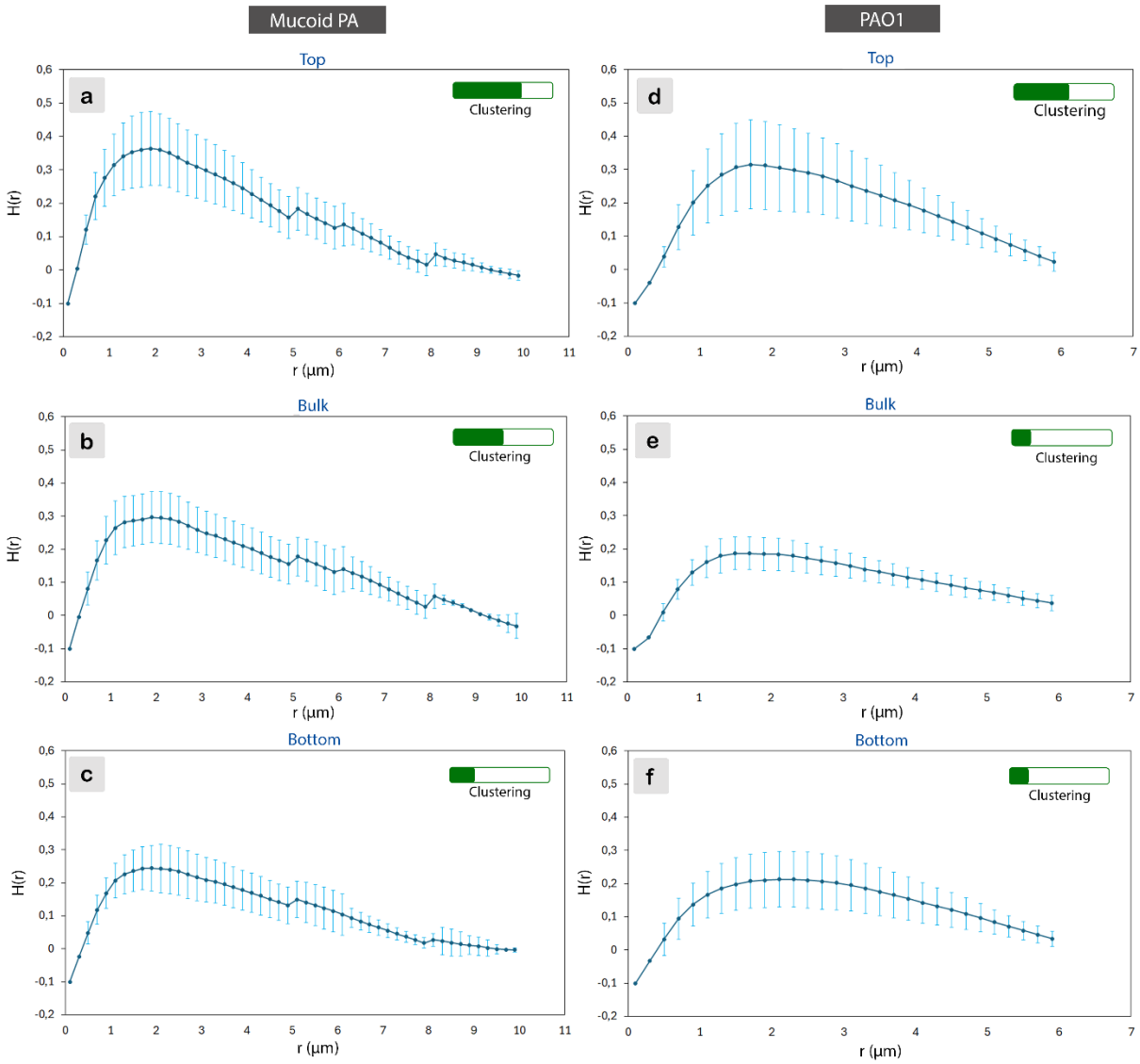

Figure 6: Spatial organization of mucoid PA and PAO1 biofilms revealed by averaged Ripley's H(r) analysis. Ripley's H(r) functions were calculated for cells located in volumes close to the a,d) biofilm–substrate interface (Bottom), b, e) in the biofilm interior (Bulk), c, f) and close to the biofilm–liquid interface (Top) for mucoid PA (left) and PAO1 (right) biofilms. Curves represent Ripley's H(r) values averaged across more than 5 independent biological replicates per strain, and the error bars signify the 95% confidence interval.

305 Mucoid PA biofilms exhibited vertically stratified spatial organization. Within the top volume, the
306 mucoid strain exhibited the highest degree of clustering, with $H(r)$ reaching peak values of ~ 0.38–
307 0.40 at r ≈ 1.5–2.0 μm, as expected. Positive $H(r)$ values persisted until $r \approx 8$ μm, indicating the
308 presence of larger clusters than in the interior of the biofilm. Within the biofilm interior (bulk
309 region), results showed less clustering, with peak $H(r)$ values of ~0.30–0.32 at $r \approx 1.5$–2.0 μm. In
310 the bottom volume, mucoid PA biofilms displayed the least clustering. Peak $H(r)$ values of
311 approximately 0.25–0.26 were observed at $r \approx 1.8$–2.2 μm.

312 $H(r)$ values up to 8 μm throughout the mucoid biofilm indicate the presence of clusters in the sense
313 of local correlations in bacterial organization. However, the RDF analysis, cryo-SEM images, and
314 $H(r)$ values of 0.2-0.4 reveal that these clusters are not densely packed microcolonies, as they might
315 appear from a cursory inspection of confocal data. CLSM visually exaggerates bacterial packing
316 through background fluorescence and diffraction-limited resolution. A possible interpretation of the
317 moderate overall clustering and the significantly higher clustering at the top of the biofilm is that
318 local clustering in young mucoid PA biofilms mainly reflects the migration of daughter cells from
319 mother cells, which is more pronounced in the biofilm's actively growing top layer. Conversely,
320 this argument suggests that cell division has largely ceased at the bottom and in the bulk biofilm.
321 From a functional perspective, clustering is expected to exacerbate diffusion limitations, promote
322 metabolic stratification, and increase tolerance to antimicrobial treatments.

323 In contrast to the mucoid strain, PAO1 biofilms exhibited weaker spatial organization and reduced
324 vertical stratification. In the top region of the biofilm, PAO1 exhibited stronger clustering than in
325 the other regions, with peak $H(r)$ values of approximately 0.31–0.32 at $r \approx 1.5$–2.0 μm. Positive
326 $H(r)$ values declined more rapidly than in the mucoid strain, approaching zero by $r \approx 6$ μm. The
327 bulk and bottom regions exhibited weaker clustering than the top layer for PAO1, with peak $H(r)$
328 values of ~ 0.18–0.19 and 0.21-0.22, respectively, at $r \approx 1.5$–2.0 μm, reflecting a more
329 homogeneous internal organization. These results indicate that while PAO1 forms signs of sparse
330 clusters, these are even less pronounced and smaller than for the mucoid strain.

331 Taken together, the cryo-SEM and CLSM analyses consistently demonstrate that cell organization
332 within 4-day-old mucoid and PAO1 biofilms is not random; it is characterized by short-range spatial
333 order, but not by strong cluster formation and microcolony formation, and by relatively large
334 spacing and a broad distribution of spacings between nearest neighbors. Hence, our data challenge
335 the conventional view of PA biofilms as tightly packed cell clusters surrounded by ECM, which
336 was mainly derived from observations of collapsed biofilms.[67–70] An analogous finding of cell-cell

spacing was reported by Kamila *et al.*, who described large distances between microbial cells in cryo-imaged *Staphylococcus epidermidis* and yeast biofilms, but did not analyze it further.[29] A locally ordered, spaced, and homogeneous distribution of distant bacterial cells in biofilms has implications for our understanding of their communication, cooperation, and migration. It has direct functional implications, as controlled cell–cell spacing and ECM continuity will influence antibiotic penetration, phage accessibility, and immune clearance, thereby contributing to the persistence of clinical PA infections.[71]

2.3 The Extracellular Matrix of PA Biofilms Exhibits Aligned Fibrillar Structures that are Strain Dependent

Different PA strains do not form the same types of biofilms.[72–74] Well-known examples include the dense biofilms formed on biomaterial surfaces, where PA acts as an opportunistic pathogen, and the mucoid biofilms formed by PA in cystic fibrosis patients.[69,75,76] Despite differences in structure and the critical role of the ECM in shaping biofilm architecture and contributing to antimicrobial resistance, a notable gap remains in our understanding of the ultrastructural organization of different types of biofilms. Electron microscopy studies on PA have focused on bacterial cell morphology, surface attachment, or overall biofilm structure.[32,77,78] Differences in internal structure between biofilms, e.g., PAO1 *vs*. mucoid PA, have not been imaged and compared in detail.

Cryo-SEM images from the top, bulk, and bottom regions of mucoid PA revealed structural differences, as shown in **Figure 7**. While the bulk region exhibited mostly locally aligned fibrils extending through the ECM (**Figure 7 b**), the top and bottom parts of the biofilm displayed a markedly different ECM morphology. The top and bottom of the biofilm were characterized by a mesh-like appearance of the ECM (**Figure 7 a and c**). Although the bottom also displayed fibrils, these were less aligned than in the bulk. We did not find such region-specific differences in ECM architecture between the top, bulk, and bottom zones of mucoid PA biofilms reported in the literature, as such differences are likely observable only using HPF freeze-fracture cryo-SEM. Despite these differences in ECM ultrastructure, the spatial organization of bacterial cells (cell-cell spacing) was similar across the strata of the biofilms.

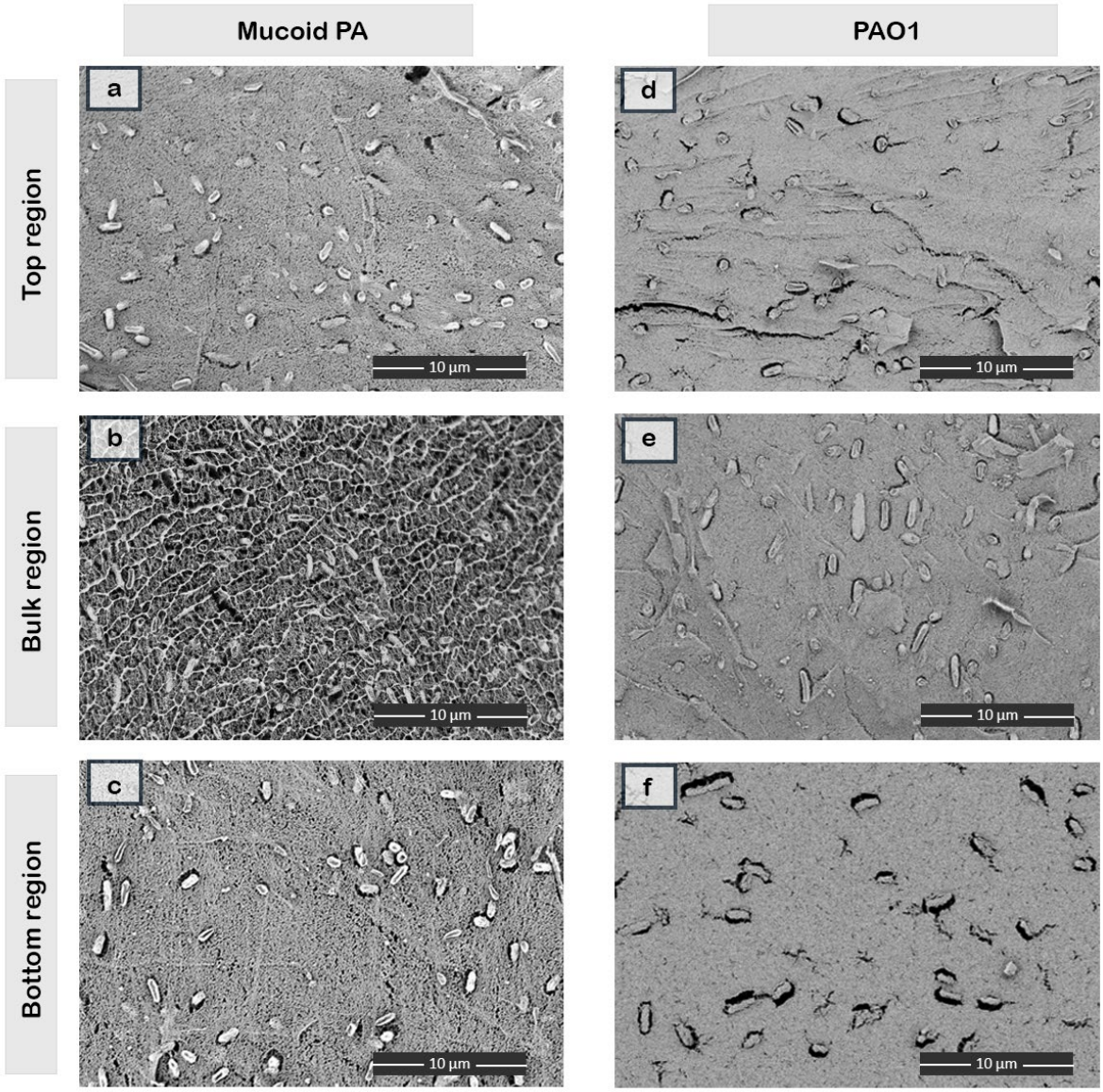

Figure 7: Cryo-SEM micrograph demonstrating variations in ECM architecture in different regions of 4-day-old mucoid and PAO1 biofilms grown on gold carriers. Micrographs shown for a) top part of the biofilm (~1–5 µm from the biofilm surface), b) bulk part of the biofilm, and c) bottom part of the biofilm (~1–5 µm from the substrate).

After observing the fibrillar organization in mucoid PA biofilms, we compared these biofilms with PAO1 biofilms to see if such structures are present. The ECM in all three regions of PAO1 biofilms presents a dense and mesh-like structure **Figure 7 d – f)**, suggesting that the aligned fibrillar organization is typical for the mucoid strain but not ubiquitously observed.

374 The observations of aligned fibrillar structures in the interior of mucoid PA biofilms but not in the
375 denser PAO1 biofilms were surprising, as the ECM in mucoid biofilms is distinguished by
376 predominantly being formed from alginate, which has more than an order of magnitude smaller
377 dimensions than the thickness and spacing of the structures observed in our images. Notably, the
378 well-ordered and aligned fibrillar features are also absent in any of the compositionally comparable
379 alginate hydrogels (**Figure 1a – c**), suggesting that these features observed in mucoid PA biofilms
380 do not arise from the alginate matrix alone. Instead, they may reflect biofilm-specific structural
381 organization involving other ECM components that self-assemble or are organized by the mucoid
382 PA during biofilm matrix synthesis.

383 While the cryo-SEM data do not allow direct assignment of biochemical identity, the contrast, size,
384 and organization of these fibrillar features are consistent with larger molecular assemblies, such as
385 bundles formed by large glycoconjugates, eDNA complexes, or protein fibers, which are known
386 ECM components of *Pseudomonas*.[79–81]

387 Several PA ECM components, including amyloid-forming proteins (e.g., Fap fibers), glycosylated
388 adhesins, and DNA polymer composites, are known to self-assemble into filamentous or fibrillar
389 structures and could possibly contribute to the observed morphology.[82–86] At the same time, it is
390 important to note that some well-characterized fibrillar matrix proteins, such as CdrA, are primarily
391 associated with Psl-rich, non-mucoid biofilms like PAO1 and may play a reduced or altered role in
392 alginate-dominated mucoid strains.[74,87] Nevertheless, strain-specific expression patterns do not fully
393 exclude their involvement, particularly in mature biofilms where multiple matrix components may
394 coexist and interact.

395 Filamentous matrix molecules are increasingly recognized as key determinants of biofilm
396 viscoelasticity and cohesion; their enrichment in the bulk suggests they are part of the load-bearing
397 scaffold that allows mucoid biofilms to resist shear and deformation.[83,88] Their formation may be
398 linked to biofilm maturation, increased matrix complexity, or mechanical confinement that may
399 promote higher-order assembly.[89,90] Ultimately, the mature, dense, cohesive volumes of biofilms
400 are where nutrient gradients, slow growth, and the highest antibiotic tolerance reside,[91,92] linking
401 matrix ultrastructure to the formation of highly protected "refuge" compartments for cells. Previous
402 studies have shown that disruption of matrix architecture through enzymatic degradation of
403 extracellular DNA, inhibition of amyloid fiber formation, or interference with polysaccharide
404 synthesis can significantly enhance antibiotic efficacy and immune clearance.[93–95]

Definitive identification of the molecular composition of observed features will require complementary biochemical, proteomic, or targeted labeling approaches, which are beyond the scope of the present study but represent important directions for future work.

2.4 Minimal Etching Preserves Mucoid Biofilm Ultrastructure, While Extended Etching Collapses It into a Mesh

To ensure that the observed fibrillar structures were not preparation artefacts, we employed controlled cryo-etching to progressively reveal the biofilm ultrastructure. Cryo-SEM imaging of PA mucoid biofilms (bulk region) subjected to varying etching times (0 s, 20 s, and 60 s) at –110 °C and ~5.6×10^{-7} mbar revealed progressive exposure of structural features (**Figure 8**). At 0 s etching, the biofilm surface appeared partially obscured by residual surface ice. Nonetheless, ECM contours (green arrow) and outlines of bacterial cells (yellow arrows) were discernible also where ice is visible (**Figure 8**a).

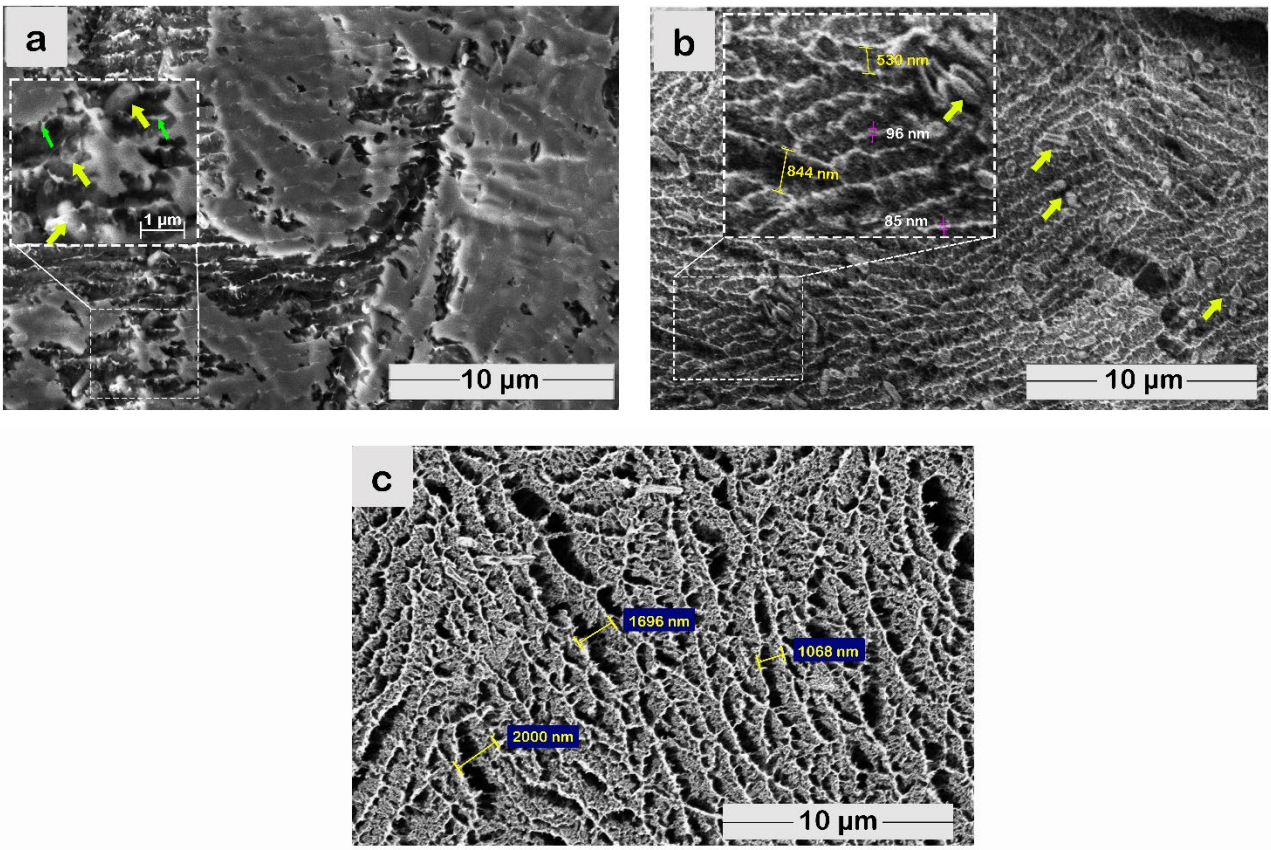

Figure 8: Cryo-SEM micrographs from the bulk region of 4-day-old mucoid PA biofilms. a) 0 s etching, b) 20 s etching, and c) deep etching (60 s). The yellow arrows indicate the outlines of bacterial cells, while the green arrows indicate the contours of the ECM.

421 Etching for 20 s at -110 °C and ~5.6×10^{-7} mbar (**Figure 8**b) produced optimal surface contrast
422 with well-preserved ultrastructure with good correspondence to the features imaged without
423 etching. PA cells were visible (yellow arrow) and embedded in the ECM. The aligned fibrillar
424 features measured 85-96 nm in width, with inter-fibrillar spacing ranging from 500 to 850 nm. This
425 etching duration appeared to achieve an effective balance between the removal of surface ice and
426 the preservation of hydrated structural features of PA biofilms.

427 In contrast, extended etching for 60 s at -110°C and ~5.6×10^{-7} mbar (**Figure 8**c) led to sublimation
428 of water to a greater depth, resulting in a more open and fibrous ECM morphology. The ECM
429 showed increased fibrillar spacing in the range of 900 to 2000 nm, indicating the onset of matrix
430 distortion and collapse. The fibrils were also less aligned and more mesh-like than after shorter
431 etching times.

432 The observed effects of freeze-etching are consistent with studies by Wan *et al*., Dohnalkova *et al.*,
433 and Garbarino *et al.*, which demonstrated that controlled etching could enhance the visualization of
434 highly organized ultrastructural ECM and cellular features.[96–98] However, they also showed that
435 extended etching times increased the risk of ECM ultrastructure alterations, which are particularly
436 severe for strongly glycosylated (hydrated) ECMs,[97,98] such as those found in mucoid PA biofilms.[99]
437 Consistently in our study and theirs,[98] water removal *via* sublimation leads to a more mesh-like
438 structure. Such mesh-like structures are commonly reported in the literature and are therefore
439 associated with biofilm ECMs. However, in a fully hydrated biofilm, water occupies the spaces
440 between ECM components, maintaining their relative positions and allowing the matrix to adopt an
441 organized architecture.[40–42] When water is removed, this spatial and energetic support is lost. As a
442 result, matrix components are drawn closer together by surface tension and intermolecular
443 interactions, leading to collapse and a mesh-like rearrangement that obscures the original
444 structure.[43,44]
445
446

447 2.5 PAO1 Biofilms Are Thinner with Higher and More Variable Cell Density than Mucoid Biofilms

448 To further quantify how bacteria organize as a function of distance from the substrate and differ
449 between mucoid and PAO1 biofilms, we grew PA biofilms on sapphire discs (for cryo-SEM) and
450 cover glass (for CLSM) to obtain a quantitative, cross-sectional view of the native biofilm thickness.
451 The discs were mounted vertically in the cryo-sample holder and fractured (**Figure S5**), allowing
452 for a cross-sectional view orthogonal to the growth surface (**Figure S6)**. This orientation exposes

453 the entire biofilm profile, from base to surface (**Figure 9**a – b), enabling direct visualization of
454 spatial features such as bacterial layering and changes in density along the biofilm depth, as well as
455 the accurate native biofilm thickness, including ECM. While this approach has been used in cryo-
456 SEM to study biofilm architecture of *Staphylococcus aureus*, *Candida parapsilosis,* and co-cultures
457 of *Staphylococcus epidermidis* and yeast,[29,47] it has not been applied to elucidate the biofilm
458 architecture of PA strains.

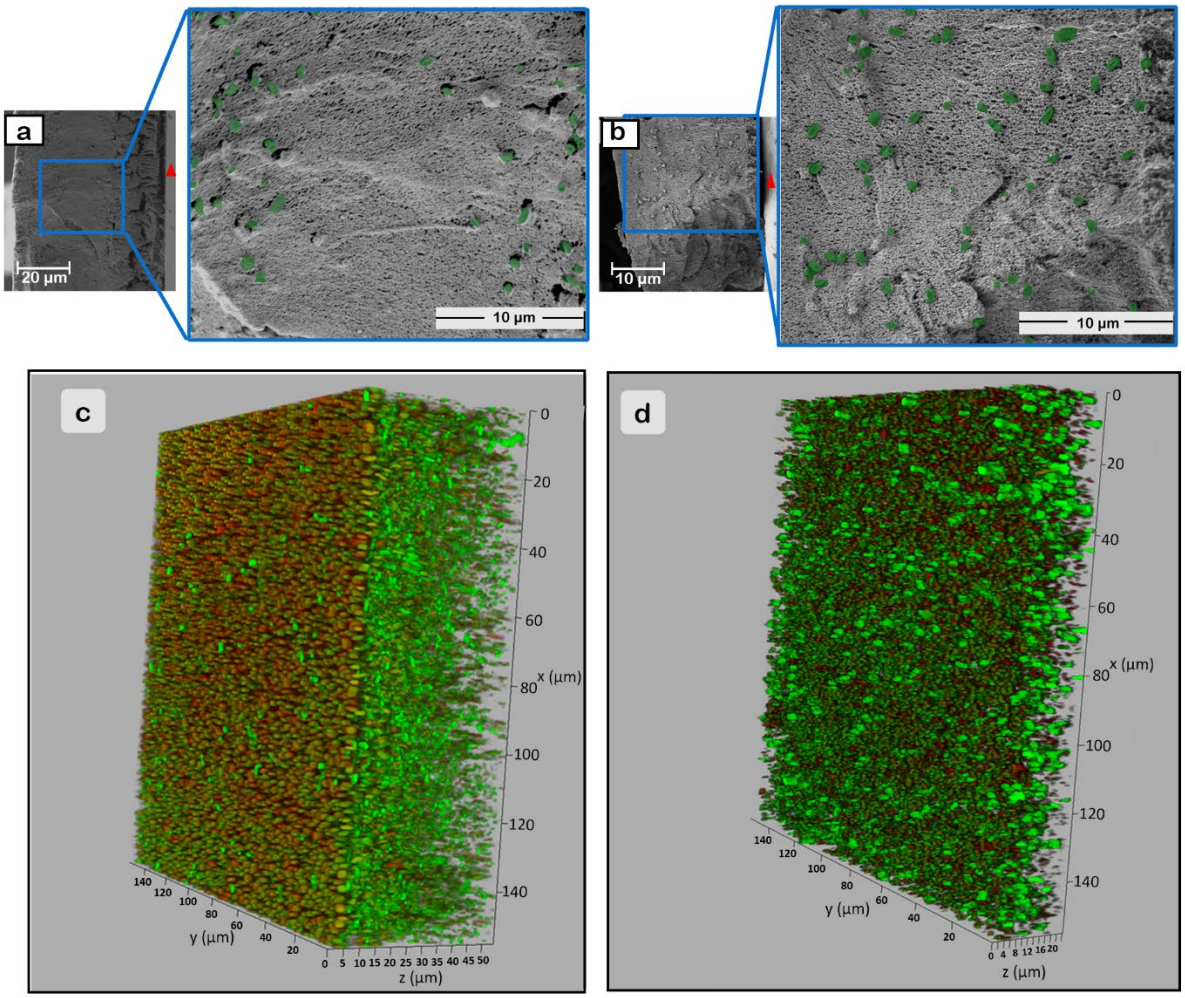

459

460 **Figure 9**: Cryo-SEM micrographs and CLSM images of PA biofilms. PA biofilms were grown on
461 sapphire discs for 4 days and subsequently high-pressure cryo-frozen and fractured orthogonally to
462 the substrate to reveal a biofilm cross-section for a) mucoid PA biofilm and b) PAO1 biofilm. The
463 red triangles point towards the disc surface (substrate). 3D CLSM stacks of c) mucoid PA and d)
464 PAO1 biofilms after 4 days of growth on microscope glass slips.

465 The cross-sectional cryo-SEM view of biofilms showed that the ECM of both PAO1 and mucoid
466 PA biofilms formed a thick, cohesive, and uniform mesh-like structure (**Figure 9**a – b). The ECM

467 enveloped the bacterial cells, embedding them within the biofilm and indicating robust matrix
468 production and structural integrity. Despite similar matrix appearances, several quantifiable
469 differences in biofilm thickness were observed between the two strains. PAO1 biofilms were
470 thinner, with a mean thickness of 26.8 ± 5.4 µm from the substrate to the top of the ECM after 4
471 days of growth. Mucoid PA biofilms were thicker (54.5 ± 4.9 µm). CLSM images, in which the
472 thickness was determined by observing fluorescent bacterial cells, yielded similar thicknesses, i.e.,
473 28.27 ± 5.93 µm and 52.88 ± 10.72 µm for PAO1 and mucoid PA, respectively, as shown in **Figure**
474 **9c and d**. A thickness difference, although less pronounced, was also observed by Nahum *et al*.,[100]
475 who documented 20% higher thicknesses of 5-day-old mucoid PA biofilms (~ 65 µm) than non-
476 mucoid PA biofilms. [69]

477 Quantitative analysis of cryo-SEM cross sections suggested vertical heterogeneity in cell density
478 within mucoid biofilms (**Figure S6**), with enrichment at the top of the biofilm interface and reduced
479 densities toward the substrate. However, these observations exhibited substantial variance and
480 inconsistent trends across regions and strains, particularly for PAO1 biofilms, for which density
481 differences were not statistically significant. Moreover, cryo-SEM provides only local 2D snapshots
482 of small areas of the biofilm. As a result, cryo-SEM–based density estimates alone may not reliably
483 capture the full three-dimensional spatial organization of cells across the biofilm depth.

484 Quantitative volumetric analysis of CLSM image stacks, therefore, provided a more robust
485 framework for assessing cell density across biofilm depth. This analysis revealed pronounced
486 spatial variability in cell density across biofilm regions. While several studies have highlighted
487 elevated bacterial densities and metabolic activities at the biofilm-nutrient source interface,[101–104] to
488 our knowledge, no study has reported the bacterial distribution throughout mucoid PA and PAO1
489 biofilms. To provide a robust statistical basis for structural comparison, the vertical occupancy
490 profile for each biofilm (**Figure 10)** was derived from the analysis of >8 independent biofilm
491 samples per strain.

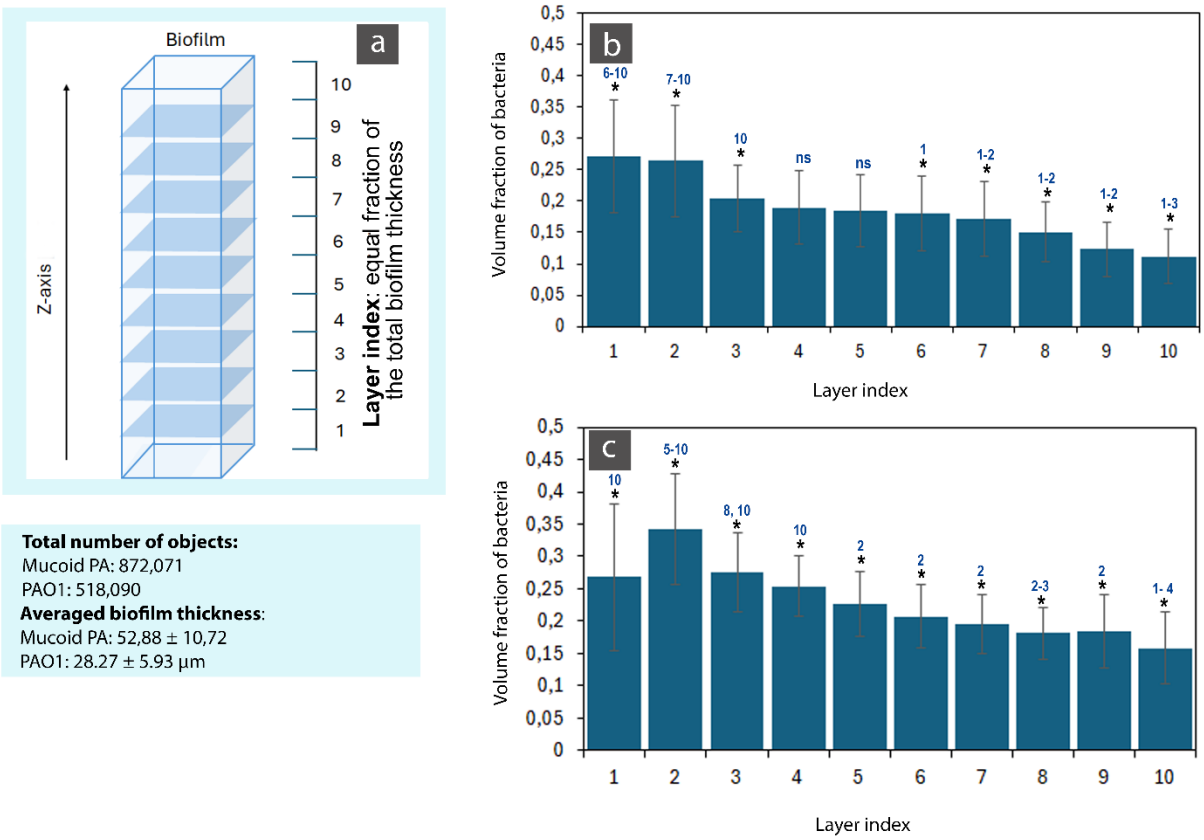

Figure 10: Vertical distribution of bacterial volume fraction across biofilm depth for *P. aeruginosa* biofilms. a) Schematic illustration of the strategy used to generate vertical volume fraction profiles in 3D biofilms. The biofilm volume was partitioned along the z-axis into 10 equally spaced layers, each corresponding to a fraction of the total biofilm thickness. For mucoid biofilms, layers were approximately ~5 µm thick, whereas PAO1 layers were ~3 µm thick, reflecting differences in overall biofilm thickness. For each layer, the volume fraction of bacteria after segmentation and cylinder fitting was calculated. These layer-resolved values were subsequently used to generate averaged vertical density profiles. Bacterial volume fractions per layer for b) mucoid PA and c) PAO1 biofilms are presented as mean ± 95% confidence interval. Statistical comparisons between layers are indicated above the bars (ns, not significant ($p \geq 0.05$); * = significant ($p \leq 0.05$)).

The total biofilm thickness was divided into 10 equally spaced layers along the z-axis (**Figure 10**a), and for each layer, the volume fraction of bacteria was calculated. Multiple datasets (>8) were averaged to generate the mean profiles shown in **Figure 10**b and c. Averaging was performed per layer, ignoring the minimal variation in biofilm and layer thickness. The resulting profiles suggest a monotonously decreasing vertical density gradient in both biofilm types. In both cases, the highest bacterial volume fractions were observed in the lower layers (layer indices 1–3), with the lower-layer bacterial density (1) significantly higher ($p \leq 0.05$) than that of the top layer (10). This

510 indicates a densely packed basal region proximal to the attachment surface, corresponding to an
511 approximately 2-fold reduction between the most densely and least densely populated layers. This
512 trend was observed in most individual biofilms analyzed, demonstrating that the vertical density
513 gradient represents a systematic structural feature rather than an artifact of averaging. Additionally,
514 the substantial variability in bacterial volume fraction within individual layers primarily reflects
515 variation in bacterial density across different biofilms.

516 The gradual reduction in bacterial density, combined with the observed differences in bacterial
517 distribution, suggests a transition from a compact core to a more porous, heterogeneous architecture
518 in the upper biofilm regions. Most quantitative studies report an increase in cell packing density
519 toward the bottom/interior of PA biofilms, while the top is less dense but more metabolically and
520 regulatory active.[51,71,77,105,106] This stratification is key to understanding persistence and treatment
521 failure. The layer-resolved, cell-based occupancy profiles obtained in this study, even for rather
522 young biofilms, provide quantitative design constraints for the development of physiologically
523 relevant 3D biofilm models. Rather than assuming uniform density or homogeneous cell
524 distributions, these data suggest that incorporating non-uniform density profiles into 3D biofilm
525 models is essential for accurately modeling PA biofilms during their formation.

526 In contrast to our expectations, the average volume fractions in the 4-day-old biofilms analyzed
527 with CLSM were similar for PAO1 and mucoid PA, i.e., 0.23 ± 0.06 and 0.19 ± 0.05, respectively
528 (**Figure S7**). Although the mucoid PA had a lower volume fraction, the difference was not
529 statistically significant ($p \geq 0.05$). With similar volume fractions but significantly thicker mucoid
530 PA biofilms, this implies significantly higher cell division in young mucoid biofilms than in PAO1
531 biofilms, and that the less elastic modulus of mucoid biofilms are mainly due to their different ECM
532 composition. We stress that although more than six biological replicates of each biofilm were
533 analyzed, larger sample sizes and observations at different time points might alter this picture.

534 Our observations are consistent with prior work showing that while mucoid *P. aeruginosa* strains
535 are thicker, overproducing EPS, particularly alginate,[6,74,100,107] PAO1 biofilms contain more
536 bacterial volume, although in our study this was only indicated and not a statistically certain
537 observation.[108] Notably, in a biofilm study, Henriksen *et al*. observed that an alginate-overproducing
538 *P. aeruginosa* mucA strain had lower bacterial volume than the non-mucoid (PAO1) strain,
539 underscoring that biofilm thickness is not a reliable measure of bacterial biomass.[108]

Overall, our results demonstrate that biofilm architecture is layer-dependent. The layered organization provides a mechanistic link between cell-level interactions, volumetric density profiles, ECM structure, and emergent biofilm properties, such as robustness, persistence, and treatment tolerance. To date, direct, depth-resolved comparisons of biofilm architecture between mucoid PA and PAO1 under comparable experimental conditions have not been reported. Nevertheless, the existing literature consistently shows that older PAO1 biofilms are structured, with Psl-rich peripheral regions and internal cavities, whereas alginate overproduction in mucoid strains is repeatedly associated with thicker, more cohesive, and more persistent biofilm matrices.[12,74,109]

3. 0 Materials and Methods

3.1 Bacterial strains, growth conditions, and antibiotics.

The *P. aeruginosa* (PA) strains utilized in this study include PAO1(ATCC 15692) and a mucoid strain (ATCC 39324). Unless otherwise specified, frozen bacterial stocks were thawed and initially cultured overnight at 37 °C in Tryptic Soy Broth (TSB). Subsequently, the bacteria were sub-cultured onto Tryptic Soy Agar (TSA) plates and incubated for 24 h. Colonies were then transferred to 10 ml of TSB and cultured at 37 °C for 16–18 h with agitation at 100 rpm to produce a bacterial suspension for further experimentation.

3.2 Biofilm Growth

Overnight cultures of PA strains (PAO1 & PA ATCC 39324) were harvested and washed 3 times with phosphate-buffered saline (PBS). The bacterial suspensions were then adjusted to an optical density at 600 nm (OD_{600}) of 0.1 in TSB. Sterile 18 x 18 mm cover glasses (thickness 1 – Carl Roth), 3 mm diameter specimen carriers (gold-coated – Type A, Leica Microsystems Inc., Austria) (**Figure S5a**) with 100 µm indentations, along with 6 mm sapphire discs (Leica Microsystems Inc., Austria) (**Figure S5b**), were placed in Petri dishes containing the respective bacterial suspensions. Unless otherwise stated, PA strains were allowed to grow for 4 days in TSB to form biofilms on these substrates by incubating them at 37 °C. Biofilms for SEM/CryoSEM were further covered with an additional 3 mm and/or 6 mm Type A carrier, carefully lined with double-sided tape to create a secure sandwich after 4 days growth prior to sample preparation.

569 **3.3 Alginate hydrogel preparation**

570 A 1.5 wt% alginate stock solution (acetylated)[9] was prepared by dissolving 150 mg alginate
571 overnight in 8 ml of sterile 0.9 wt% NaCl solution (solvent). Then, the solvent was added to the
572 mixture to achieve a final volume of 10 mL, which was used as the stock solution. For alginate gels
573 containing bacteria, the stock solution was diluted with 0.9 wt% NaCl and PAO1 liquid culture to
574 obtain a 0.5 wt% alginate solution as ink with a defined PA concentration (0.1 OD).
575 Approximately 150 µl of PA-containing and control (without PA) alginate solutions were then
576 placed in disc-shaped agarose molds. To prepare agarose molds, 2 g of agarose powder (Sigma)
577 was mixed with 1.47 g of $CaCl_2$ in 100 mL of Milli-Q water and then autoclaved. The agarose molds
578 were gelled to a height of 3 mm and punctured with 7-mm-diameter punches. For alginate hydrogel
579 fabrication, the punched spaces in the agarose molds were filled with PA-containing and control
580 alginate solutions, respectively. The solutions were left to crosslink in the agarose molds at room
581 temperature for 1 h. After gelling, the hydrogels were washed three times with 0.9 wt% NaCl.
582 Hydrogels with PA were incubated in $CaCl_2$-supplemented TSB overnight at 37 °C under shaking
583 at 100 rpm.

584 **3.4 Sample Preparation for SEM Imaging**

585 *3.4.1 Air/HDMS Drying and Scanning Electron Microscope Imaging of Samples*

586 Alginate hydrogels and PA biofilms, after incubation, were subjected to chemical fixation by
587 immersion in a 2.5% glutaraldehyde solution (Sigma) and left overnight at 4 °C. Following fixation,
588 the samples underwent two consecutive rinses with a 0.9 wt% sodium chloride (NaCl) solution,
589 followed by sequential dehydration in ethanol solutions of increasing concentrations: 30%, 50%,
590 70%, 90%, 95%, and finally, 100%, all conducted at room temperature for 3 min each.
591 Subsequently, the chemically fixed samples were treated with 100% hexamethyldisilazane (HMDS)
592 for 1 min and air-dried. Prior to air-drying, biofilms grown on sample carriers were manually
593 fractured using a clean blade to expose internal structures. Alginate hydrogel samples, with or
594 without embedded bacteria, were sectioned into halves using a clean blade after air-drying.
595 Similarly, biofilms grown on glass substrates were carefully cut into smaller sections following air-
596 drying to facilitate subsequent imaging. All samples were uniformly sputter-coated (Leica EM
597 SCD005, Leica, Germany) with a ~8 nm thick layer of gold to enhance sample conductivity and
598 image contrast. SEM imaging was carried out using an Apreo VS SEM (Thermo Scientific, The
599 Netherlands) at an acceleration voltage of 5.0 kV and a current of 0.10 nA. High vacuum back-
600 scattered and secondary electrons were detected using T1 and T2 in-lens detectors, respectively.

601 *3.4.2 Critical-point Drying and Scanning Electron Microscope Imaging of Samples*

602 Alginate hydrogels and PA biofilms were subjected to chemical fixation and dehydration as
603 described above. Subsequently, samples were transitioned to acetone (Sigma) as the intermediary
604 solvent before drying using a critical-point dryer (Leica EM CPD030, Leica, Germany). Biofilms
605 grown on sample carriers and alginate hydrogel samples were manually fractured using a clean
606 blade to expose internal structures after CPD. Biofilms grown on glass substrates were carefully cut
607 into smaller sections before CPD to accommodate the dimensions of the drying chamber. All
608 samples were subsequently coated with ~8 nm of gold and then imaged with SEM (Apreo VS SEM,
609 Thermo Scientific, The Netherlands).

610 *3.4.3 Cyro Preparation and Scanning Electron Microscope Imaging of Samples*

611 Selected samples were high-pressure frozen using the Leica EM HPM100 (Leica Microsystems
612 Inc., Austria). More specifically, for PA-containing and empty alginate hydrogels, ~80–100 µm
613 thick slices were cut with a sterile scalpel and transferred to the bottom carrier using forceps and
614 then sandwiched with a top carrier. For PA biofilms, samples on the 3 mm Type A carriers were
615 gently covered with matching top carriers to create a secure sandwich. The sapphire discs with
616 biofilms were placed (biofilm side up) into the indentation of a 6 mm Type A carrier. A spacer was
617 added on top to prevent movement and ensure even contact. The assembly is completed by placing
618 a matching top carrier over the disc to create a secure sandwich.

619 All sandwiched carriers are immediately loaded into the HPM100 high-pressure freezer and
620 automatically frozen according to the protocol described in Garbarino et al.[98] The frozen samples
621 are afterwards discharged into a liquid nitrogen-filled Dewar for preservation before being
622 transferred to the freeze-fracture system under cryogenic conditions. The frozen sample carriers or
623 sapphire discs were mounted onto the sample holder under liquid nitrogen (LN_2) and transferred to
624 a Leica EM ACE900 (Leica Microsystems Inc., Austria) freeze-fracture system. Freeze-fracturing
625 was performed at -120 °C using a flat-edge knife.
626 Unless otherwise stated, to enhance structural visibility of fractured samples, sublimation (etching)
627 was performed for 20 s at –110 °C under a vacuum of ~5.6×10^{-7} mbar. While a standard etching
628 time of 20 s was applied for most samples, selected samples were also subjected to 0 s (no
629 sublimation) and extended 60 s etching times. This approach enabled the assessment of surface
630 exposure of the ECM and bacterial structure.
631 Following the sublimation step, the fractured samples were e-beam coated with a 4-nm platinum
632 layer at a 45° angle and a 4-nm carbon layer at a 90° angle to improve contrast and minimize beam

damage during imaging. Subsequently, the samples were transferred to SEM via a cryo-transfer system (Leica EM VCT500).

Cryo-SEM imaging was performed using the Apreo VS SEM (Thermo Scientific, The Netherlands) at an operating voltage of 1.0 kV and a current of 0.10 nA in a high vacuum mode. Backscattered and secondary electrons were detected via the in-lens T1 and T2 detectors, respectively. Throughout the imaging process, the SEM chamber temperature was maintained between -110 °C and -120 °C, depending on the chamber pressure to avoid sublimation and condensation, as observed *in situ*.

For each imaging technique, more than three independent samples were prepared. From each sample, a minimum of 10 fields of view were imaged, and representative images were selected based on the preservation of sample structures. Where applicable, bacterial cells were manually false-coloured green using Adobe Photoshop (version 25.5.3).

3.5 Sample Preparation for CLSM

Alginate hydrogels and *P. aeruginosa* biofilms (on cover glasses) were prepared for confocal laser scanning microscopy (CLSM) following incubation under the conditions described above. To preserve biofilm structure while enabling fluorescence imaging, samples were gently handled throughout preparation.

Biofilms and alginate hydrogels (with bacteria) were stained using a Live/Dead BacLight bacterial viability kit (Thermo Fisher Scientific) according to the manufacturer's instructions. Following staining, the hydrogel samples were rinsed gently with sterile 0.9 wt% sodium chloride solution to remove excess dye. In contrast, rinsing of PA biofilms grown on cover glasses was avoided to prevent shear-induced disruption and loss of loosely attached cells; instead, excess staining solution was carefully removed from the staining chamber by pipetting.

For volumetric imaging, alginate hydrogel samples (with bacteria) were carefully sliced in half using a clean, sharp blade to expose internal regions. Slicing was performed immediately prior to imaging. Biofilms grown on cover glasses were imaged directly without sectioning.

Alginate hydrogel samples were placed in glass-bottom Petri dishes (35 mm), whereas biofilms grown on cover glasses were overlaid with an additional coverslip to prevent evaporation during CLSM acquisition. Imaging was performed using a Leica TCS SP8-STED inverted microscope.

3.6 Quantitative Spatial Analysis of *Pseudomonas* Biofilm Structure

3.6.1 Cryo-SEM Data Processing

Cryo-SEM images were analyzed consistently using a custom Python script applied to the overlay images derived from the cryo-SEM datasets. Individual bacterial cells were first manually masked (**Figure 11**), as the dense and heterogeneous biofilm architecture precluded reliable automated cell detection using standard image analysis software (e.g., ImageJ) or commonly used segmentation algorithms. The manually masked images served as the input for subsequent computational analysis.

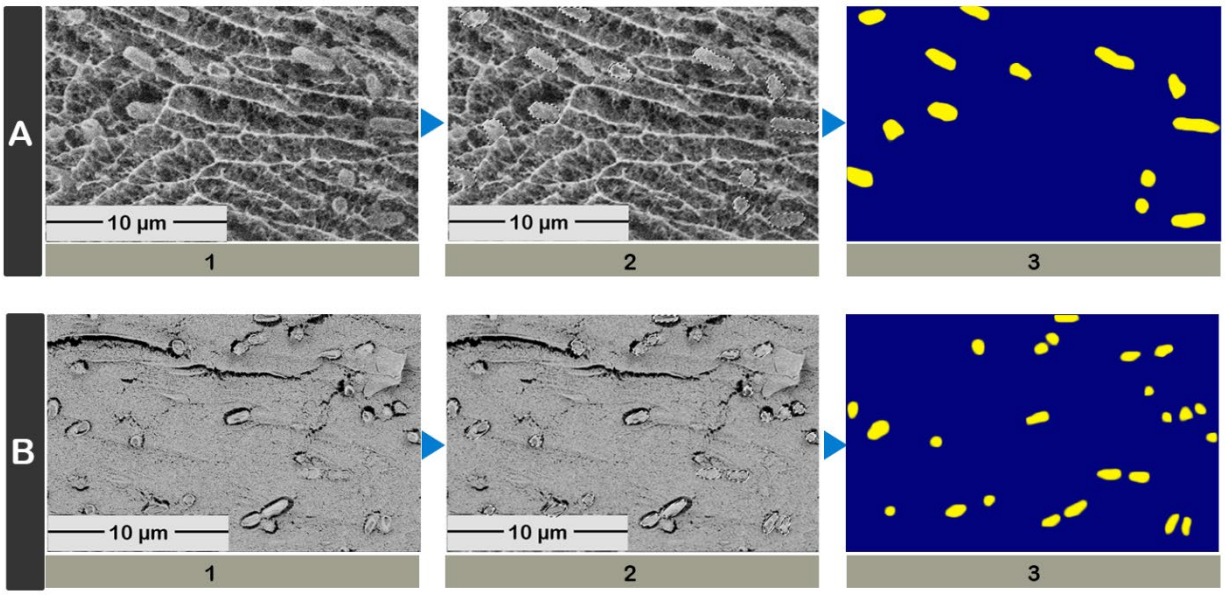

Figure 11: Workflow for cryoSEM image processing and extraction of bacteria for spatial analysis. (1) Representative cryo-SEM images of PA biofilms (A and B) showing native ECM architecture and embedded bacterial cells. (2) Manually masked bacterial cells. (3) Masked bacterial cells following color thresholding.

To isolate bacterial shapes, the Python script applied a color-based threshold to identify the yellow hue corresponding to the masked bacteria. The resulting pixel binary masks were subjected to a morphological opening operation (dilation followed by erosion) to remove small artifacts, suppress noise, and smooth object boundaries prior to spatial analysis. Geometric features were then extracted by identifying contours within the processed binary masks. For each contour, the script fitted an ellipse to determine the centroid coordinates, major axis length, minor axis thickness, and orientation angle of each bacterium. The extracted centroid coordinates were subsequently used for spatial analyses.

682 *3.6.2 CLSM Data Processing*

683 CLSM data were analyzed consistently, without manual steps, using a custom-made Python script
684 applied to the raw voxel fluorescence-intensity data from each biofilm measurement. In brief, an
685 intensity threshold was applied to the combined fluorescence intensity of the live and dead channels
686 to isolate bacterial signals from background noise for each voxel. Bacteria were identified by
687 segmenting the merged fluorescence signals using a Watershed algorithm. A cylindrical-shape
688 constraint was used, requiring a cylindrical shape with maximum and minimum lengths and radial
689 dimensions, defined by compiling histograms of bacterial dimensions for PAO1 and mucoid PA,
690 respectively, from cryo-SEM data for each strain and adding the microscopy point-spread functions
691 in x, y, and z, respectively. The cylinders were fitted using weighted principal component analysis,
692 accounting for the intensity of individual voxels rather than a simple binary mask. Bacteria with
693 overlapping fluorescence signals were separated by recursively splitting objects, rejecting too thin
694 objects, and forcing splitting by halving the length of objects if they are outside of the shape
695 constraints after reaching the maximum depth of the Watershed algorithmic splitting. The resulting
696 data on bacteria annotated with cylinders were overlaid on the raw fluorescence data for
697 classification based on their fractions of live and dead fluorescence, and their spatial distributions
698 were used to calculate centroids and volumes for statistical analysis of CLSM data.

699 *3.6.3 Radial Distribution Function (RDF) and Nearest-Neighbor Distance Analyses*

700 To assess cell–cell spacing in PA biofilms, the RDF (with Monte Carlo correction – **equation 1**),
701 defined as the normalized probability density of finding a neighbor at distance *r* from a reference
702 particle, compared to a random distribution, was calculated from data obtained from the processed
703 cryo-SEM (2D radial coordinates) and CLSM (cylindrical coordinates) images, respectively.

704 $$g(r) = \frac{H_{obs}(r)}{H_{rand}(r)} \times \frac{N_{rand}}{N_{obs}} \quad (1)$$

705 Python scripts calculated the nearest-neighbor distances, defined as the Euclidean distance from
706 each bacterium's centroid to that of its closest neighbour in 2D for cryo-SEM data and in 3D for
707 CLSM data.

708 RDFs from datasets of the same sample type (strain and imaging technique) were aggregated, and
709 the mean $g(r)$ was calculated together with the 95% confidence intervals, assuming a Student's t-
710 distribution. Nearest-neighbour distances were summarized as histograms, from which mean and
711 modal (peak) values were extracted.

712 *3.6.4 Vertical Cell Density Profiling*

713 To evaluate how cell density varied with distance from the substrate, cryo-SEM images of fractured
714 biofilms grown on sapphire discs were analyzed. Each image was divided into horizontal
715 rectangular regions of interest (ROIs) (**Figure S6a – b**), aligned parallel to the substrate. For mucoid
716 biofilms, ROI widths were set to 5 µm, while for PAO1 biofilms, a width of 4 µm was used to
717 accommodate differences in biofilm structure and cell density. Cell counts within each ROI were
718 manually determined in Adobe Photoshop, ensuring consistent and accurate quantification. The
719 constant area across ROIs enabled direct calculation of cell density (cells per μm^2) as a function of
720 distance from the substrate.

721 Additionally, vertical cell-density profiles were derived from 3D CLSM image stacks to quantify
722 the spatial distribution of bacterial cells along the biofilm thickness. Within the entire analyzed
723 volume, bacterial cells (fitted cylinders) were identified using intensity-based segmentation
724 described above. The total biofilm thickness was divided into 10 equally spaced layers along the z-
725 axis, and, for each layer, the volume fraction of cylinders fitted as bacteria was calculated. Multiple
726 datasets (>8) from both PA strains were subsequently averaged to generate the mean profiles.
727 Averaging was performed layer by layer, ignoring the minimal variation in biofilm and layer
728 thickness. Layer-resolved volume fractions were aligned by layer index, as all datasets were
729 discretized into the same number of Z layers.

730 For statistical evaluation, mean density and 95% Confidence Interval (CI) were calculated for each
731 bin. One-way ANOVA with Tukey and LSD post hoc tests was performed to determine significant
732 differences in cell density across depths. (IBM SPSS Statistics (27.0.1)). A p-value ≤ 0.05 was
733 considered statistically significant.

734 3.6.5 *Ripley's H(r) spatial analysis*

735 Clustering of bacteria in biofilm was quantified using Ripley's $H(r)$ function (equation 2).

736 $$K(r) = \int_0^r g(r')4\pi(r')^2 dr' \,;\; L(r) = \left(\frac{K(r)}{\frac{4}{3}\pi}\right)^{1/3} \,;\; H(r) = L(r) - r \qquad (2)$$

737 To assess depth-dependent organization, biofilms were subdivided into three volume regions based
738 on their vertical position: the biofilm–substrate interface (Bottom), the biofilm interior (Bulk), and
739 the biofilm–liquid interface (Top). Each was designated as 20% of the biofilm thickness in the
740 corresponding region: 0-20% (Bottom), 40-60% (Bulk), and 80-100% (Top). Ripley's H-function
741 was calculated for each region. $H(r) \approx 0$ indicates random spatial organization, positive $H(r)$ values

742 indicate clustering, negative $H(r)$ values indicate spatial inhibition or regularity, and the peak in H
743 gives an approximate cluster radius.

744 To ensure robust comparison between strains, Ripley's $H(r)$ functions were averaged across at least
745 six independent biological replicates per strain. All analyses were performed using Python scripts
746 on the centroid positions of bacteria identified in the 3D confocal data.

747 *3.6.6 Pore Size Distribution of Acetylated Alginate Prepared by Different Methods*

748 SEM micrographs of the acetylated alginate samples prepared by air-drying, CPD, and cryo
749 methods were taken at similar magnifications to ensure consistent pore size measurements. Pore
750 size analysis was conducted using ImageJ (**Figure S8**). The resulting datasets were imported into
751 RStudio (version R4.3.1, R Foundation for Statistical Computing) for statistical analysis and
752 visualization. Pore size distributions for each preparation method were visualized using boxplots,
753 generated with the ggplot2 package, to illustrate the variation in pore dimensions across sample
754 groups. Results were additionally analyzed using one-way ANOVA with Tukey and LSD post hoc
755 tests (IBM SPSS Statistics (27.0.1)), to determine significant differences.

756 **4. Conclusion**

757 Using a cryo-SEM workflow, we revealed 4-day-old *Pseudomonas* biofilms as highly hydrated,
758 spatially organized structures, with individual bacteria distinctly embedded within the extracellular
759 matrix. The imaged structures stood in stark contrast to the dense, clustered bacterial arrangements
760 reported for samples prepared by conventional air-drying or critical-point drying methods.

761 By quantitative analysis of cryo-SEM and CLSM images, we determined that PA biofilms exhibit
762 weak short-range order throughout the biofilm. Furthermore, we demonstrated that the bacterial
763 volume fraction was highest near the substrate, but that bacterial clustering was stronger at the top
764 of the biofilm. Importantly, throughout the biofilm, bacteria were clearly separated, typically by
765 large amounts of ECM, as shown by cryo-SEM images, nearest-neighbor distance distributions, and
766 calculations of the RDF and Ripley's H-function, challenging the view that, especially mucoid, PA
767 biofilms contain densely packed microcolonies.

768 Mucoid PA differed markedly from PAO1 biofilms, reaching twice the thickness in 4 days despite
769 a lower bacterial volume fraction in the outermost, actively growing biofilm layer. They also
770 showed more pronounced clustering at the top of the biofilm than PAO1, despite their lower volume
771 fraction, suggesting that the observed clustering is primarily due to incomplete daughter-cell
772 migration.

Finally, we imaged aligned fibrillar structures in the bulk of mucoid PA biofilms. Such structures were found in neither alginate hydrogels nor in PAO1 biofilms. We suggest that they originate from proteins, such as amyloid fibrils or large glycoconjugates, that self-assemble within the alginate-rich matrix during maturation; however, further analyses are needed to confirm this hypothesis.

It is important to note that these observations reflect structural features of biofilms grown in rich nutrient medium (TSB) and should not be overgeneralized to other environments, such as minimal media or *in vivo* settings (e.g., the lung). ECM production is metabolically demanding, and reduced nutrient availability may significantly alter matrix composition, density, and organization. While experimental investigation of these effects lies beyond the scope of the present work, we view this as an important direction for future studies using the imaging workflow we have established.

Our study highlights the critical importance of selecting appropriate sample-preparation methods to accurately visualize native biofilm structures, and the potential of cryo-SEM, combined with CLSM, as a quantitative tool for biofilm analysis, owing to its preservation of native features and distances. Importantly, cryo-SEM can provide insights into the considerable structural variability in biofilm organization that we demonstrate persists even between strains.

Acknowledgement and Funding

This project was supported by the BOKU Core Facility Multiscale Imaging. We thank the FWF Austrian Science Fund for funding (P33226).

Code Availability

The underlying custom Python codes for this study are not yet publicly available but may be made available to qualified researchers on reasonable request from the corresponding author.

References

1. H⃠iby, N., Ciofu, O. & Bjarnsholt, T. *Pseudomonas Aeruginosa* Biofilms in Cystic fibrosis. *Future Microbiol.* **5**, 1663–1674 (2010).
2. Wei, Q. & Ma, L. Biofilm Matrix and Its Regulation in Pseudomonas aeruginosa. *Int. J. Mol. Sci.* **14**, 20983–21005 (2013).
3. Thi, M. T. T., Wibowo, D. & Rehm, B. H. A. Pseudomonas aeruginosa Biofilms. *Int. J. Mol. Sci.* **21**, 8671 (2020).
4. Guillaume, O., Butnarasu, C., Visentin, S. & Reimhult, E. Interplay between biofilm microenvironment and pathogenicity of Pseudomonas aeruginosa in cystic fibrosis lung chronic infection. *Biofilm* vol. 4 Preprint at https://doi.org/10.1016/j.bioflm.2022.100089 (2022).
5. Ghafoor, A., Hay, I. D. & Rehm, B. H. A. Role of Exopolysaccharides in Pseudomonas aeruginosa Biofilm Formation and Architecture. *Appl. Environ. Microbiol.* **77**, 5238–5246 (2011).
6. Kundukad, B., Rice, S. A., Doyle, P. S. & Kjelleberg, S. Alginate exopolymer significantly modulates the viscoelastic properties and resilience of bacterial biofilms. *NPJ Biofilms Microbiomes* **11**, 98 (2025).
7. Hentzer, M. *et al.* Alginate Overproduction Affects *Pseudomonas aeruginosa* Biofilm Structure and Function. *J. Bacteriol.* **183**, 5395–5401 (2001).
8. Boyd, A. & Chakrabarty, A. M. Pseudomonas aeruginosa biofilms: role of the alginate exopolysaccharide. *J. Ind. Microbiol.* **15**, 162–168 (1995).
9. Schandl, S. *et al.* Acetylation of alginate enables the production of inks that mimic the chemical properties of P. aeruginosa biofilm. *J. Mater. Chem. B* https://doi.org/10.1039/d4tb02675f (2025) doi:10.1039/d4tb02675f.
10. Shree, P., Singh, C. K., Sodhi, K. K., Surya, J. N. & Singh, D. K. Biofilms: Understanding the structure and contribution towards bacterial resistance in antibiotics. *Medicine in Microecology* **16**, 100084 (2023).
11. Sharma, S. *et al.* Microbial Biofilm: A Review on Formation, Infection, Antibiotic Resistance, Control Measures, and Innovative Treatment. *Microorganisms* **11**, 1614 (2023).
12. Hentzer, M. *et al.* Alginate Overproduction Affects *Pseudomonas aeruginosa* Biofilm Structure and Function. *J. Bacteriol.* **183**, 5395–5401 (2001).

833 13. Wozniak, D. J. *et al.* Alginate is not a significant component of the extracellular
834 polysaccharide matrix of PA14 and PAO1 *Pseudomonas aeruginosa* biofilms. *Proceedings of*
835 *the National Academy of Sciences* **100**, 7907–7912 (2003).
836 14. Osondu-Chuka, G. O. *et al.* Beyond the matrix: rethinking antibiotic tolerance in CF biofilms
837 using 3D models. *NPJ Biofilms Microbiomes* **12**, 3 (2025).
838 15. Guzmán-Soto, I. *et al.* Mimicking biofilm formation and development: Recent progress in
839 in vitro and in vivo biofilm models. *iScience* **24**, 102443 (2021).
840 16. Highmore, C. J. *et al.* Translational challenges and opportunities in biofilm science: a BRIEF
841 for the future. *NPJ Biofilms Microbiomes* **8**, 68 (2022).
842 17. Sønderholm, M. *et al.* Tools for studying growth patterns and chemical dynamics of
843 aggregated Pseudomonas aeruginosa exposed to different electron acceptors in an alginate
844 bead model. *NPJ Biofilms Microbiomes* **4**, 3 (2018).
845 18. Li, S. *et al.* Hierarchical biofilm models using sodium alginate beads containing bacteria
846 embedded in a cellulose–chitosan hydrogel matrix. *J. Mater. Chem. B* **13**, 3952–3958 (2025).
847 19. Cao, B. *et al.* Antibiotic penetration and bacterial killing in a *Pseudomonas aeruginosa*
848 biofilm model. *Journal of Antimicrobial Chemotherapy* **70**, 2057–2063 (2015).
849 20. Park, J. *et al.* Direct Observation of Wet Biological Samples by Graphene Liquid Cell
850 Transmission Electron Microscopy. *Nano Lett.* **15**, 4737–4744 (2015).
851 21. Ogura, T. Direct observation of unstained biological samples in water using newly developed
852 impedance scanning electron microscopy. *PLoS One* **14**, e0221296 (2019).
853 22. Lyu, Z., Yao, L., Chen, W., Kalutantirige, F. C. & Chen, Q. Electron Microscopy Studies of Soft
854 Nanomaterials. *Chem. Rev.* **123**, 4051–4145 (2023).
855 23. Asker, D. *et al.* Preventing *Pseudomonas aeruginosa* Biofilms on Indwelling Catheters by
856 Surface-Bound Enzymes. *ACS Appl. Bio Mater.* **4**, 8248–8258 (2021).
857 24. Manabe, K., Nishizawa, S. & Shiratori, S. Porous Surface Structure Fabricated by Breath
858 Figures that Suppresses *Pseudomonas aeruginosa* Biofilm Formation. *ACS Appl. Mater.*
859 *Interfaces* **5**, 11900–11905 (2013).
860 25. Sugimoto, S. *et al.* Imaging of bacterial multicellular behaviour in biofilms in liquid by
861 atmospheric scanning electron microscopy. *Sci. Rep.* **6**, 25889 (2016).
862 26. Relucenti, M. *et al.* Microscopy Methods for Biofilm Imaging: Focus on SEM and VP-SEM
863 Pros and Cons. *Biology (Basel).* **10**, 51 (2021).

864 27. Asahi, Y. *et al.* Simple observation of Streptococcus mutans biofilm by scanning electron
865 microscopy using ionic liquids. *AMB Express* **5**, 6 (2015).
866 28. Alleman, J. E., Russell, E. K., Lantz, W. L. & Wukasch, R. F. Biofilm cryopreparation for
867 scanning electron microscopy. *Water Res.* **19**, 1073–1078 (1985).
868 29. Hrubanova, K., Nebesarova, J., Ruzicka, F. & Krzyzanek, V. The innovation of cryo-SEM
869 freeze-fracturing methodology demonstrated on high pressure frozen biofilm. *Micron* **110**,
870 28–35 (2018).
871 30. Fleeman, R. M., Mikesh, M. & Davies, B. W. Investigating Klebsiella pneumoniae biofilm
872 preservation for scanning electron microscopy. *Access Microbiol.* **5**, (2023).
873 31. SCHAUDINN, C. *et al.* Imaging of endodontic biofilms by combined microscopy (FISH/cLSM
874 – SEM). *J. Microsc.* **235**, 124–127 (2009).
875 32. Priester, J. H. *et al.* Enhanced visualization of microbial biofilms by staining and
876 environmental scanning electron microscopy. *J. Microbiol. Methods* **68**, 577–587 (2007).
877 33. Lawrence, J. R. *et al.* Scanning Transmission X-Ray, Laser Scanning, and Transmission
878 Electron Microscopy Mapping of the Exopolymeric Matrix of Microbial Biofilms. *Appl.*
879 *Environ. Microbiol.* **69**, 5543–5554 (2003).
880 34. Kher, L., Kelley, K. & Santoro, D. Ultrastructural Analysis of Differences in the Growth and
881 Maturation of Staphylococcus pseudintermedius Biofilm on Biotic and Abiotic Surfaces.
882 *Microbiol. Spectr.* **11**, (2023).
883 35. Zhang, Y. *et al.* Challenges and current advances in in vitro biofilm characterization.
884 *Biotechnol. J.* **18**, (2023).
885 36. Fratesi, S. E., Lynch, F. L., Kirkland, B. L. & Brown, L. R. Effects of SEM Preparation Techniques
886 on the Appearance of Bacteria and Biofilms in the Carter Sandstone. *Journal of Sedimentary*
887 *Research* **74**, 858–867 (2004).
888 37. Kang, K.-Y. *et al.* Critical Point Drying: An Effective Drying Method for Direct Measurement
889 of the Surface Area of a Pretreated Cellulosic Biomass. *Polymers (Basel).* **10**, 676 (2018).
890 38. Dassanayake, R. P. *et al.* Identification of a reliable fixative solution to preserve the complex
891 architecture of bacterial biofilms for scanning electron microscopy evaluation. *PLoS One* **15**,
892 e0233973 (2020).
893 39. Karcz, J., Bernas, T., Nowak, A., Talik, E. & Woznica, A. Application of lyophilization to
894 prepare the nitrifying bacterial biofilm for imaging with scanning electron microscopy.
895 *Scanning* **34**, 26–36 (2012).

896 40. Johnson, E. *et al.* Correlative in-resin super-resolution and electron microscopy using
897 standard fluorescent proteins. *Sci. Rep.* **5**, 9583 (2015).
898 41. McCutcheon, J. & Southam, G. Advanced biofilm staining techniques for TEM and SEM in
899 geomicrobiology: Implications for visualizing EPS architecture, mineral nucleation, and
900 microfossil generation. *Chem. Geol.* **498**, 115–127 (2018).
901 42. Hrubanova, K., Nebesarova, J., Ruzicka, F. & Krzyzanek, V. The innovation of cryo-SEM
902 freeze-fracturing methodology demonstrated on high pressure frozen biofilm. *Micron* **110**,
903 28–35 (2018).
904 43. Ichihashi, S., Kuwata, M., Kikuchi, K., Matsuyama, T. & Shimizu, A. Optimization of method
905 for cross-section hydrogels preparation using high-pressure freezing. *Microscopy* **73**, 430–
906 438 (2024).
907 44. KRISTENSEN, G. & CHRISTENSEN, F. Application of cryo-cut method for measurements of
908 biofilm thickness. *Water Res.* **16**, 1619–1621 (1982).
909 45. Webster, P., Wu, S., Webster, S., Rich, K. A. & McDonald, K. Ultrastructural preservation of
910 biofilms formed by non-typeable *Hemophilus influenzae*. *Biofilms* **1**, 165–182 (2004).
911 46. Wan, P. *et al.* Cryo-SEM Investigation of Chlorella Using Filter Paper
912 as Substrate. *Bio. Protoc.* **14**, (2024).
913 47. Krzyzanek, V., Hrubanova, K., Nebesarova, J. & Ruzicka, F. Cryo-SEM of Perpendicular Cross
914 Freeze-Fractures Through a High-Pressure-frozen Biofilm. *Microscopy and Microanalysis* **20**,
915 1232–1233 (2014).
916 48. Ben-Sahil, A., Mohamed, A. & Beyenal, H. Three-dimensional biofilm image reconstruction
917 for assessing structural parameters. *Biotechnol. Bioeng.* **117**, 2460–2468 (2020).
918 49. Mueller, L. N., de Brouwer, J. F., Almeida, J. S., Stal, L. J. & Xavier, J. B. Analysis of a marine
919 phototrophic biofilm by confocal laser scanning microscopy using the new image
920 quantification software PHLIP. *BMC Ecol.* **6**, 1 (2006).
921 50. Neu, T. R. & Lawrence, J. R. Investigation of Microbial Biofilm Structure by Laser Scanning
922 Microscopy. in 1–51 (2014). doi:10.1007/10_2014_272.
923 51. Lawrence, J. R., Korber, D. R., Hoyle, B. D., Costerton, J. W. & Caldwell, D. E. Optical
924 sectioning of microbial biofilms. *J. Bacteriol.* **173**, 6558–6567 (1991).
925 52. Hirai, N. *et al.* Three-Dimensional Structure of Biofilm Formed on Glass Surfaces Revealed
926 Using Scanning Ion Conductance Microscopy Combined with Confocal Laser Scanning
927 Microscopy. *Microorganisms* **13**, 1779 (2025).

928 53. Hartmann, R. *et al.* Quantitative image analysis of microbial communities with BiofilmQ.
929 *Nat. Microbiol.* **6**, 151–156 (2021).
930 54. Zhang, J. *et al.* BCM3D 2.0: accurate segmentation of single bacterial cells in dense biofilms
931 using computationally generated intermediate image representations. *NPJ Biofilms*
932 *Microbiomes* **8**, 99 (2022).
933 55. Fratesi, S. E., Lynch, F. L., Kirkland, B. L. & Brown, L. R. *EFFECTS OF SEM PREPARATION*
934 *TECHNIQUES ON THE APPEARANCE OF BACTERIA AND BIOFILMS IN THE CARTER*
935 *SANDSTONE*. *JOURNAL OF SEDIMENTARY RESEARCH* vol. 74 (2004).
936 56. Osondu-Chuka O.G., S. S. , S. A. , G. O. , O. A. , R. E. Beyond the Matrix: Rethinking Antibiotic
937 Tolerance in CF Biofilms Using 3D Models. *Advance Healthcare Materials* (2025).
938 57. Sønderholm, M. *et al.* Pseudomonas aeruginosa Aggregate Formation in an Alginate Bead
939 Model System Exhibits *In Vivo* -Like Characteristics. *Appl. Environ. Microbiol.* **83**, (2017).
940 58. Wright, B. *et al.* Enhanced Viability of Corneal Epithelial Cells for Efficient Transport/Storage
941 Using a Structurally Modified Calcium Alginate Hydrogel. *Regenerative Med.* **7**, 295–307
942 (2012).
943 59. Schandl, S. *et al.* Synthetically acetylated alginate is a superior in vitro biofilm model for
944 antibiotic testing showing reduced tobramycin affinity. *Eur. Polym. J.* **237**, 114176 (2025).
945 60. Jabalameli, F., Emaneini, M., Beigverdi, R., Halimi, S. & Siroosi, M. Determining effects of
946 nitrate, arginine, and ferrous on antibiotic recalcitrance of clinical strains of Pseudomonas
947 aeruginosa in biofilm-inspired alginate encapsulates. *Ann. Clin. Microbiol. Antimicrob.* **22**,
948 61 (2023).
949 61. Yang, Z., Khan, S. A., Walsh, L. J., Ziora, Z. M. & Seneviratne, C. J. Classical and Modern
950 Models for Biofilm Studies: A Comprehensive Review. *Antibiotics* **13**, 1228 (2024).
951 62. Langton Hewer, S. C., Smith, S., Rowbotham, N. J., Yule, A. & Smyth, A. R. Antibiotic
952 strategies for eradicating Pseudomonas aeruginosa in people with cystic fibrosis. *Cochrane*
953 *Database of Systematic Reviews* **2023**, (2023).
954 63. Azeredo, J. *et al.* Critical review on biofilm methods. *Crit. Rev. Microbiol.* **43**, 313–351
955 (2017).
956 64. Alhede, M. *et al.* Combination of microscopic techniques reveals a comprehensive visual
957 impression of biofilm structure and composition. *FEMS Immunol. Med. Microbiol.* **65**, 335–
958 342 (2012).

959 65. Kraevsky, S. V. *et al.* Using the Radial Distribution Function to Analyze Atomic Force
960 Microscopy Images of Colloidal Systems. *Int. J. Mol. Sci.* **26**, 210 (2024).
961 66. Thorneywork, A. L., Roth, R., Aarts, D. G. A. L. & Dullens, R. P. A. Communication: Radial
962 distribution functions in a two-dimensional binary colloidal hard sphere system. *J. Chem.*
963 *Phys.* **140**, (2014).
964 67. Li, D. *et al.* Biofilm Formation by Pseudomonas aeruginosa in a Novel Septic Arthritis Model.
965 *Front. Cell. Infect. Microbiol.* **11**, (2021).
966 68. Yang, Y. *et al.* Inactivation of Pseudomonas aeruginosa Biofilms by 405-Nanometer-Light-
967 Emitting Diode Illumination. *Appl. Environ. Microbiol.* **86**, (2020).
968 69. Lee, K. & Yoon, S. S. Pseudomonas aeruginosa Biofilm, a Programmed Bacterial Life for
969 Fitness. *J. Microbiol. Biotechnol.* **27**, 1053–1064 (2017).
970 70. Brandenburg, K. S. *et al.* Development of *Pseudomonas aeruginosa* Biofilms in Partial-
971 Thickness Burn Wounds Using a Sprague-Dawley Rat Model. *Journal of Burn Care &*
972 *Research* **40**, 44–57 (2019).
973 71. Dayton, H. *et al.* Cellular arrangement impacts metabolic activity and antibiotic tolerance in
974 Pseudomonas aeruginosa biofilms. *PLoS Biol.* **22**, e3002205 (2024).
975 72. Płókarz, D., Czopowicz, M., Bierowiec, K. & Rypuła, K. Virulence Genes as Markers for
976 Pseudomonas aeruginosa Biofilm Formation in Dogs and Cats. *Animals* **12**, 422 (2022).
977 73. Maurice, N. M., Bedi, B. & Sadikot, R. T. *Pseudomonas aeruginosa* Biofilms: Host Response
978 and Clinical Implications in Lung Infections. *Am. J. Respir. Cell Mol. Biol.* **58**, 428–439 (2018).
979 74. Jacobs, H. M. *et al.* Mucoid Pseudomonas aeruginosa Can Produce Calcium-Gelled Biofilms
980 Independent of the Matrix Components Psl and CdrA. *J. Bacteriol.* **204**, (2022).
981 75. Thi, M. T. T., Wibowo, D. & Rehm, B. H. A. Pseudomonas aeruginosa Biofilms. *Int. J. Mol. Sci.*
982 **21**, 8671 (2020).
983 76. Yin, R., Cheng, J., Wang, J., Li, P. & Lin, J. Treatment of Pseudomonas aeruginosa infectious
984 biofilms: Challenges and strategies. *Front. Microbiol.* **13**, (2022).
985 77. Hunter, R. C. & Beveridge, T. J. High-Resolution Visualization of *Pseudomonas aeruginosa*
986 PAO1 Biofilms by Freeze-Substitution Transmission Electron Microscopy. *J. Bacteriol.* **187**,
987 7619–7630 (2005).
988 78. Wilking, J. N., Angelini, T. E., Seminara, A., Brenner, M. P. & Weitz, D. A. Biofilms as complex
989 fluids. *MRS Bull.* **36**, 385–391 (2011).

990 79. Nahum, Y., Cerrone, A. & Nerenberg, R. Impact of Low-Frequency Ultrasound on Physical
991 Properties and Antibiotic Susceptibility of a Mucoid Biofilm. *Langmuir* **41**, 6718–6728
992 (2025).
993 80. Zeng, G. *et al.* Functional bacterial amyloid increases Pseudomonas biofilm hydrophobicity
994 and stiffness. *Front. Microbiol.* **6**, (2015).
995 81. Bleem, A. *et al.* Protein Engineering Reveals Mechanisms of Functional Amyloid Formation
996 in Pseudomonas aeruginosa Biofilms. *J. Mol. Biol.* **430**, 3751–3763 (2018).
997 82. Blanco-Romero, E. *et al.* Role of extracellular matrix components in biofilm formation and
998 adaptation of Pseudomonas ogarae F113 to the rhizosphere environment. *Front. Microbiol.*
999 **15**, (2024).
1000 83. Seviour, T. *et al.* The biofilm matrix scaffold of Pseudomonas aeruginosa contains G-
1001 quadruplex extracellular DNA structures. *NPJ Biofilms Microbiomes* **7**, 27 (2021).
1002 84. Akbey, Ü. & Andreasen, M. Functional amyloids from bacterial biofilms – structural
1003 properties and interaction partners. *Chem. Sci.* **13**, 6457–6477 (2022).
1004 85. Reichhardt, C. The Pseudomonas aeruginosa Biofilm Matrix Protein CdrA Has Similarities to
1005 Other Fibrillar Adhesin Proteins. *J. Bacteriol.* **205**, (2023).
1006 86. Ferguson, D. L., Gloag, E. S., Parsek, M. R. & Wozniak, D. J. Extracellular DNA enhances
1007 biofilm integrity and mechanical properties of mucoid *Pseudomonas aeruginosa*. *J.*
1008 *Bacteriol.* **205**, (2023).
1009 87. Reichhardt, C. *et al.* The Versatile Pseudomonas aeruginosa Biofilm Matrix Protein CdrA
1010 Promotes Aggregation through Different Extracellular Exopolysaccharide Interactions. *J.*
1011 *Bacteriol.* **202**, (2020).
1012 88. Böhning, J., Tarafder, A. K. & Bharat, T. A. M. The role of filamentous matrix molecules in
1013 shaping the architecture and emergent properties of bacterial biofilms. *Biochemical Journal*
1014 **481**, 245–263 (2024).
1015 89. David, A. *et al.* Pseudomonas aeruginosa Biofilm Lifecycle: Involvement of Mechanical
1016 Constraints and Timeline of Matrix Production. *Antibiotics* **13**, 688 (2024).
1017 90. Mann, E. E. & Wozniak, D. J. *Pseudomonas* biofilm matrix composition and niche biology.
1018 *FEMS Microbiol. Rev.* **36**, 893–916 (2012).
1019 91. Jo, J., Price-Whelan, A. & Dietrich, L. E. P. Gradients and consequences of heterogeneity in
1020 biofilms. *Nat. Rev. Microbiol.* **20**, 593–607 (2022).

1021 92. Roberts, M. E. & Stewart, P. S. Modeling Antibiotic Tolerance in Biofilms by Accounting for
1022 Nutrient Limitation. *Antimicrob. Agents Chemother.* **48**, 48–52 (2004).
1023 93. Bleem, A. *et al.* Designed α-sheet peptides disrupt uropathogenic E. coli biofilms rendering
1024 bacteria susceptible to antibiotics and immune cells. *Sci. Rep.* **13**, 9272 (2023).
1025 94. Kim, J.-S., Lim, M.-C., Kim, S.-M. & Lee, J.-Y. Extracellular matrix-degrading enzymes as a
1026 biofilm control strategy for food-related microorganisms. *Food Sci. Biotechnol.* **32**, 1745–
1027 1761 (2023).
1028 95. Cordisco, E., Zanor, M. I., Moreno, D. M. & Serra, D. O. Selective inhibition of the amyloid
1029 matrix of Escherichia coli biofilms by a bifunctional microbial metabolite. *NPJ Biofilms*
1030 *Microbiomes* **9**, 81 (2023).
1031 96. Wan, P. *et al.* Cryo-SEM Investigation of Chlorella Using Filter Paper
1032 as Substrate. *Bio. Protoc.* **14**, (2024).
1033 97. Dohnalkova, A. C. *et al.* Imaging Hydrated Microbial Extracellular Polymers: Comparative
1034 Analysis by Electron Microscopy. *Appl. Environ. Microbiol.* **77**, 1254–1262 (2011).
1035 98. Garbarino, E., Subbiahdoss, G., Scheberl, A., Reimhult, E. & Misevic, G. The native glycocalyx
1036 ultrastructure in humans and sponges is a self-assembled, lamellar micro- and nanoarray.
1037 *Commun. Biol.* **7**, 1677 (2024).
1038 99. Hills, O. J., Smith, J., Scott, A. J., Devine, D. A. & Chappell, H. F. Cation complexation by
1039 mucoid Pseudomonas aeruginosa extracellular polysaccharide. *PLoS One* **16**, e0257026
1040 (2021).
1041 100. Nahum, Y., Cerrone, A. & Nerenberg, R. Impact of Low-Frequency Ultrasound on Physical
1042 Properties and Antibiotic Susceptibility of a Mucoid Biofilm. *Langmuir* **41**, 6718–6728
1043 (2025).
1044 101. Werner, E. *et al.* Stratified Growth in *Pseudomonas aeruginosa* Biofilms. *Appl. Environ.*
1045 *Microbiol.* **70**, 6188–6196 (2004).
1046 102. Sternberg, C. *et al.* Distribution of Bacterial Growth Activity in Flow-Chamber Biofilms. *Appl.*
1047 *Environ. Microbiol.* **65**, 4108–4117 (1999).
1048 103. Wentland, E. J., Stewart, P. S., Huang, C.-T. & McFeters, G. A. Spatial Variations in Growth
1049 Rate within Klebsiella pneumoniae Colonies and Biofilm. *Biotechnol. Prog.* **12**, 316–321
1050 (1996).
1051 104. Xu, K. D., McFeters, G. A. & Stewart, P. S. Biofilm resistance to antimicrobial agents.
1052 *Microbiology (N Y).* **146**, 547–549 (2000).

1053 105. Peyton, B. M. Effects of shear stress and substrate loading rate on Pseudomonas aeruginosa
1054 biofilm thickness and density. *Water Res.* **30**, 29–36 (1996).
1055 106. Pérez-Osorio, A. C., Williamson, K. S. & Franklin, M. J. Heterogeneous *rpoS* and *rhlR* mRNA
1056 Levels and 16S rRNA/rDNA (rRNA Gene) Ratios within *Pseudomonas aeruginosa* Biofilms,
1057 Sampled by Laser Capture Microdissection. *J. Bacteriol.* **192**, 2991–3000 (2010).
1058 107. Sarkisova, S., Patrauchan, M. A., Berglund, D., Nivens, D. E. & Franklin, M. J. Calcium-Induced
1059 Virulence Factors Associated with the Extracellular Matrix of Mucoid *Pseudomonas*
1060 *aeruginosa* Biofilms. *J. Bacteriol.* **187**, 4327–4337 (2005).
1061 108. Henriksen, K. *et al.* P. aeruginosa flow-cell biofilms are enhanced by repeated phage
1062 treatments but can be eradicated by phage–ciprofloxacin combination. *Pathog. Dis.* **77**,
1063 (2019).
1064 109. Ramsey, D. M. & Wozniak, D. J. Understanding the control of *Pseudomonas aeruginosa*
1065 alginate synthesis and the prospects for management of chronic infections in cystic fibrosis.
1066 *Mol. Microbiol.* **56**, 309–322 (2005).
1067